ACADEMIC PRESS

Available online at www.sciencedirect.com

SCIENCE DIRECT®

Journal of Computational Physics 184 (2003) 435–475

JOURNAL OF COMPUTATIONAL PHYSICS

www.elsevier.com/locate/jcp

Axisymmetric vortex method for low-Mach number, diffusion-controlled combustion

Issam Lakkis, Ahmed F. Ghoniem *

Department of Mechanical Engineering, Massachusetts Institute of Technology, Room 3-342, 77 Massachusetts Avenue, Cambridge, MA 02139-4307, USA

Received 27 February 2002; received in revised form 30 September 2002; accepted 14 October 2002

Abstract

A grid-free, Lagrangian method for the accurate simulation of low-Mach number, variable-density, diffusion-controlled reacting flow is presented. A fast-chemistry model in which the conversion rate of reactants to products is limited by the local mixing rate is assumed in order to reduce the combustion problem to the solution of a convection–diffusion–generation equation with volumetric expansion and vorticity generation at the reaction fronts. The solutions of the continuity and vorticity equations, and the equations governing the transport of species and energy, are obtained using a formulation in which particles transport conserved quantities by convection and diffusion. The dynamic impact of exothermic combustion is captured through accurate integration of source terms in the vorticity transport equations at the location of the particles, and the extra velocity field associated with volumetric expansion at low Mach number computed to enforced mass conservation. The formulation is obtained for an axisymmetric geometry where the impact of radial symmetry is imposed partly through the introduction of an "adaptive" core function, used in the discretization of the vorticity field, whose shape depend on the location of the computational element with respect to the axis of symmetry, and partly through the implementation of the Green's functions of the Poisson's equation and the diffusion equation. The core function is used to compute the velocity field, and in the simulation of diffusion, where the formulation allows different computational elements to have different core sizes, using an extension of the vorticity redistribution approach. A fractional-step method is applied to decouple the convection and diffusion operators in the equations in the nonreacting flow. In the reacting flow simulations, operator splitting is applied to decouple the convection, generation and diffusion operators, while a second-order predictor–corrector integration is used in the convection and generation steps. Numerical tests are used to examine the convergence rates of the algorithm using a number of generic examples.

Keywords: Axisymmetric vortex method; Low-Mach number; Diffusion-controlled combustion

* Corresponding author. Tel.: 1-617-253-2295; Fax: 1-617-253-5981.
E-mail address: ghoniem@mit.edu (A.F. Ghoniem).

0021-9991/02/$ - see front matter
PII: S0021-9991(02)00030-X

1. Introduction

Lagrangian, grid-free solutions of the vorticity transport equation for incompressible and low Mach number compressible flows, known broadly as vortex methods, are particularly suited for the simulation of unsteady flows at high Reynolds numbers. Vortex methods, in different incarnations, have been suggested and applied to external and internal flows, and their pros and cons have been analyzed and demonstrated in a number of publications (for a recent survey, see [1]). Noteworthy among the pros are: the adaptivity of the time-dependent simulations as the computational point transporting vorticity are moved with the flow field, the lack of numerical diffusion, and the opportunity to avoid the "mesh tyranny" of grid based Eulerian methods. As to the cons, the method in its primitive form is $O(N^2)$, where N is the number of computational elements, the relative complexity of applying the boundary conditions, and the difficulty in implementing more complex physical processes such as nonlinear diffusion. Extension of these methods to more complex flows, e.g., buoyancy driven flows and nonuniform density flows [2,3], especially at the inviscid limits, have been successful, and for some simplified models of reacting flow, special methods have been proposed. Hybrid methods that combine a vortex solution of the Navier–Stokes equations and a finite-difference solution of the energy and chemical species transport equations have also been proposed for combustion simulations [4]. While still under development, these methods have shown success in several unique applications.

The success of vortex methods in capturing the large-scale dynamics of essentially inviscid, vorticity dominated flow has been, at the same time, a blessing and a curse! On the one hand, it has been possible, using different constructions of vortex methods, which were tailored to the flow of interest, to simulate with relative ease flows that are relatively difficult to compute using conventional methods [5–7]. On the other hand, and partly due to this success, the method has been regarded by some practitioners in the field as a "vortex model" which cannot be made to solve directly of the Navier–Stokes equations, in the sense on converging to the solution of the equations as the numerical parameters are refined. Especially in three-dimensional flows, these nearly inviscid flow simulations may be regarded as a form of large-eddy simulation where the small vorticity scales are removed or suppressed by the numerical discretization or through some small-scale suppression mechanism [8], with little negative impact on the ability of the method to capture the large-scale dynamics. This, however, is the choice of the practitioner as one can indeed choose to apply a more rigorous formulation in which both the convection and diffusion processes are simulated accurately, and allowing for the time dependent proliferation of small scale, at the cost of increasing the computational cost of the simulation. That last choice would lead to a "direct" simulation that can be shown to converge to the exact solution of NS equations as the numerical parameters are refined, and to agree with exact or other solutions of the governing equations.

One of the primary objectives of this paper is to demonstrate that, when properly constructed, a vortex method can be shown to be a solution of the Navier–Stokes solution, even at a relatively small Reynolds numbers when diffusion plays an important role. Another objective is to demonstrate that expected convergence rates can indeed be achieved if the numerical resolution refined and the coupling between the different transport processes are accurately implemented. Another objective is to show that a rather straight forward extension of the method can be used to integrate other convection–diffusion equations which govern the transport of "scalar", e.g., nonreactive chemical species which diffuse into a bulk medium while being convected with it. The compatibility of the two algorithms, that is a vortex solution of the Navier–Stokes equations and a particle method solution of the scalar transport equation improves the overall efficiency of the simulations since convection of vorticity and scalar is done in a single step. Finally, it is shown that the method can be used to solve a compressible low Mach number flow model for combustion, where volumetric expansion due to the conversion of reactants into products leads to the local acceleration of the flow, and the interaction between the pressure gradients and the density gradients acts a source of extra vorticity. The coupling between the equations in this case makes it necessary to use a prediction–correction method.

The focus of the paper is on axisymmetric flows, and hence axisymmetric vortex and particle methods. While the flow is essentially two-dimensional, it possesses some of the attributes of three-dimensional flows that makes it more interesting than planar two-dimensional flows. Moreover, due to the presence of an axis of symmetry, the choice of the core function is more challenging and requires special care. Previous formulation of axisymmetric vortex methods have been suggested by, among others, Sod [9] and Martins and Ghoniem [10], where a semistatistical solution of the diffusion equation was used, Rivoalen and Huberson [11], where the axisymmetric form of the PSC method and the diffusion velocity method were implemented (other contributions to axisymmetric vortex methods will be made in the text). In this work, the diffusion equation is solved using the redistribution method [12,13] modified to account for the presence of a finite core. The same core function used to represent the vorticity distribution of a vortex element in convection is also used in the diffusion process. We focus on demonstrating the convergence of the convection–diffusion method, and illustrate how it can be extended to the low Mach number reacting flow simulations.

The paper is organized as follows. In Section 2, the formulation of the combustion problem in an axisymmetric domain is presented with emphasis on the assumptions related to the transport coefficients and the combustion model. The fast chemistry model is used to simplify the governing equations and instead of integrating the chemical source terms, new conserved scalar variables are introduced. In Section 3, the formulations of the different numerical schemes are presented, with emphasis on the core function of the vortex ring elements, the diffusion algorithm and how the introduction of a core function impacts the equations. The formulation of the variable density continuity equation is discussed in the same section, and the treatment of the coupling between the different governing equations is discussed. In Section 4, applications of these numerical algorithms to a number of increasingly complex examples are used to study their accuracy and convergence; exact solution and finite difference solutions are used for comparison. Finally concluding remarks and future work are briefly discussed.

2. Formulation

The governing equations for an axisymmetric reacting flow at low Mach number, under the approximations listed below are, respectively, the conservation of mass, momentum, chemical species, energy, and the equation of state (for a comprehensive reference, see [14]):

$$\frac{\mathrm{D}\rho}{\mathrm{D}t} + \rho\nabla\cdot\vec{u} = 0, \tag{1}$$

$$\rho\frac{\mathrm{D}\vec{u}}{\mathrm{D}t} = -\nabla p + \frac{1}{R_e}\nabla^2\vec{u} - \rho i_z, \tag{2}$$

$$\rho\frac{\mathrm{D}Y_k}{\mathrm{D}t} = \frac{1}{L_e P_r}\nabla^2 Y_k + \Lambda_k w_f, \tag{3}$$

$$\rho\frac{\mathrm{D}T}{\mathrm{D}t} = \frac{1}{P_r}\nabla^2 T + Q_f w_f \tag{4}$$

and

$$\rho T = \frac{1}{\sum_{k=1}^{K} Y_k/W_k}. \tag{5}$$

The definitions of the variables are: t is time, ρ is density, the velocity has two components: u is in the radial, r-direction, and v is in the axial, z-direction, $\vec{u} = (u, v)$, we take z to be the vertical direction with unit vector i_z, p is pressure, Y_k is the mass fraction of a of the chemical species such that ρY_k is the mass of that species per unit volume, $k = 1,K$, w_f is the rate of formation/consumption of fuel per unit volume due to the chemical reaction (it is taken as a positive quantity, while the mass stoichiometric coefficient, Λ_k, determines whether the rate is for formation, $\Lambda_k > 0$, or consumption, $\Lambda_k < 0$), T is temperature such that $\rho c_p T$ is the enthalpy per unit volume, where c_p is the specific heat at constant pressure, W_k is the molecular weight, and K is the total number of chemical species. The variables in these equations are normalized with respect to a suitably selected parameters, namely, a length scale, r_o, and a velocity scale, $U_o = \sqrt{r_o g}$ (since, in this paper, we use this formulation to simulate a gravity driven flow), time scale r_o/U_o, free stream density and temperature, ρ_o and T_o, pressure scale, $\rho_o U_o^2$, with Q_f, the enthalpy of reaction per unit mass of fuel is normalized with respect to $c_p T_o$ (because of the definition of w_f, Q_f is taken as a positive quantity as well), and $R_e = \rho_o U_o r_o/\mu$, $P_e = U_o r_o/\alpha$ and $L_e = \alpha/D$, being the Reynolds, Peclet, and Lewis numbers, respectively, where α is the thermal diffusivity and D is the material diffusivity. The total derivative has the usual definition:

$$\frac{\mathrm{D}}{\mathrm{D}t} = \frac{\partial}{\partial t} + \left(\vec{u} \cdot \nabla\right),$$

the gradient

$$\nabla = \left(\frac{\partial}{\partial r} i_r, \frac{\partial}{\partial z} i_z\right),$$

and the Laplacian

$$\nabla^2 = \frac{\partial^2}{\partial r^2} + \frac{1}{r}\frac{\partial}{\partial r} + \frac{\partial^2}{\partial z^2}.$$

The chemical reaction, assumed to be single step and irreversible, accounts for the consumption of the reactants; the fuel (f) and the oxidant (o), in the presence of a diluent (d), and the formation of products (p) according to the following stoichiometry

$$\upsilon'_f X_f + \upsilon'_o X_o + \upsilon'_d X_d \rightarrow \upsilon''_p X_f + \upsilon''_d X_d, \tag{6}$$

where υ'_k is the molar stoichiometry of the reactants and υ''_k is that of the products, the mass stoichiometric coefficients in the species transport equations are: $\Lambda_f = -1$, $\Lambda_o = -(\upsilon'_o W_o)/(\upsilon'_f W_f) = -\varphi$, $\Lambda_p = 1 + \varphi$, and $\Lambda_d = 0$. For a diluent, which does not participate in the chemical reactions, $\upsilon'_d = \upsilon''_d$.

Following the low Mach number approximation, the "thermodynamic pressure" in the equation of state is taken to be spatially uniform, and in this unconfined flow (neglecting $\mathrm{O}(M^2)$ variations), it is temporally invariant as well. This is equivalent to assuming that the flow is "inelastic", i.e. the density is only allowed to change due to temperature variations associated with heat addition via the chemical reaction and/or other transport processes that conducts heat away form the high temperature zones, but not as function of the pressure. In fact, as will be shown in detail next, the equation of state is used to update the density according to the changes in the temperature and species concentration, both evaluated from their corresponding transport equations (see [15] for more detail). The total density variation is then used in the mass conservation equation to determine the divergence of the velocity field, one of two components of the total velocity. Decoupling the spatial variation of the pressure and density is tantamount to assuming that acoustic wave velocity is much faster than the flow velocity, and hence, pressure discontinuities are not allowed in this flow. Pressure variations, nevertheless, contribute to the momentum balance and are retained in Eq. (2). Changes in the average molecular weight due to the chemical reaction are retained in the

equation of state, and impact the temperature–density relation in Eq. (5). Note also that we do not use a Boussinesq approximation in the momentum equation, and instead allow for arbitrary density variation, which, in typical combustion problems, can reach 8:1 (e.g., for stoichiometric hydrocarbon combustion in air). Strong density variation leads to restrictions on the time steps used in the computations, and more computational points are used in areas where the spatial density gradients are steep.

One important feature of reacting flows is the variation of the viscosity and the diffusion coefficients with temperature. This is neglected in this work in order to simplify the treatment of the diffusion terms in the conservation equations. We have recently extended the diffusion algorithm to allow for variable diffusion coefficients (nonlinear diffusion) and plan to publish these results in the future. In this paper, however, we focus on demonstrating the convergence of the combustion scheme where the coupled equations are solved simultaneously without addressing the complexity of nonlinear diffusion. We have also assumed that all the species diffusion coefficients are equal, and that the constant-pressure specific heat is constant. These assumptions can be relaxed without adding much complexity to the formulation, as will be shown on latter publications. Implicit in the formulation is also neglecting the Soret and Defour effects, and the assumption that all species diffuse in the bulk (which is the diluent). These assumptions, while restrictive, do not significantly modify the essential physics of combustion.

The "vortex" based solution of Eqs. (1)–(5) is obtained following two significant steps, in which the momentum equation is replaced with vorticity transport equation, and the chemical species transport equations are replaced with an equation governing the transport of a conserved scalar, assuming that the chemical reaction is much faster than the transport processes. In the first, we obtain the vorticity-transport equation by taking the curl of Eq. (2), and noting that for this flow, $\vec{\omega} = \omega i_\theta$, and $\omega = (\partial u/\partial z) - (\partial v/\partial r)$ (with positive vorticity being in the clockwise direction). The resulting equation, after using the continuity and momentum equations, is

$$\rho\left[\frac{\partial\omega}{\partial t} + \left(\vec{u}\cdot\nabla\right)\omega - \left(\frac{u}{r} - \nabla\cdot\vec{u}\right)\omega\right] = -\left(a_z\frac{\partial\rho}{\partial r} - a_r\frac{\partial\rho}{\partial z}\right) + \frac{1}{R_e}\left(\nabla^2\omega - \frac{\omega}{r^2}\right), \tag{7}$$

where

$$a_r = \frac{\mathrm{D}u}{\mathrm{D}t} \quad \text{and} \quad a_z = \left(1 + \frac{\mathrm{D}v}{\mathrm{D}t}\right).$$

The first term on the right-hand side (RHS) corresponds to vorticity generation due to baroclinic effects, that is, due to the acceleration of fluid elements in a finite density gradient.

In the second step, we formulate a conserved scalar equation which models diffusion controlled combustion. In this work we are interested in a particular class of combustion problems in which, initially and/or upstream of the combustion zone, fuel and oxidizer flow in separately as two distinct streams, as in jet diffusion flames, reacting mixing layers or fires. In these phenomena, burning occurs only after fuel and oxidizer mix at the molecular level at a ratio determined by chemical stoichiometry, φ, followed by an "ignition delay period" defined by the chemical reaction rate. For high temperature reactions, the latter is much shorted than diffusion time scales, and hence the burning rate is determined by the rate at which the fuel and oxidizer mix by diffusion. These phenomena are known to be high Damkohler number problems, where the latter is the ratio between the diffusion time scale and the chemical reaction time scale. In such cases, the reaction zone, where the fuel and oxidizer concentrations are nonzero, remain much thinner than other length scales because the chemical reaction tend to consume the mixture of fuel and oxidizer soon after it is formed. In the limit of extremely fast reactions, the reaction zone is infinitely thin, i.e., the fuel and oxidizer never coexit, and that simplifies the analysis considerably.

One approach to solving problems in which the chemical reaction is much faster than the transport processes, is to define a Schvab–Zeldovich, "conserved species"

$$\eta_1 = Y_o - \varphi Y_f \tag{8}$$

for which, as can be seen from the governing equations and the definition of the stoichiometric coefficients, the transport equation is devoid of a chemical source term, that is;

$$\rho \frac{\mathrm{D}\eta_1}{\mathrm{D}t} = \frac{1}{L_e P_r} \nabla^2 \eta_1, \tag{9}$$

i.e., this Schvab–Zeldovich variable is a conserved "species" whose evolution is governed by convection and diffusion only. The advantage of using this variable is as follows. In the case of a truly fast reaction, as soon as the reacting species interdiffuse, i.e. mix at the molecular scale, they react forming products, i.e. reactants cannot coexist but over a very small "interfacial" zone on the order of magnitude of the diffusion thickness of the flow, and for a very short period of time, the time for the chemical reaction to proceed. Thus, in this case and at the limit of "infinitely" fast reaction, $Y_o Y_f = 0$, and the reaction surface (line in a two-dimensional model) can be defined by the equation

$$\eta_1(\vec{x}, t) = 0. \tag{10}$$

Moreover, on one side of the reaction surface, the oxidizer side, the conserved scalar reduces to $\eta_1 = Y_o$, while on the other, fuel side, $\eta_1 = -\varphi Y_f$. Thus, one needs only to solve a single species transport equation for a conserved scalar to determine the location of the reaction front separating fuel and the oxidizer, and the distribution of the both reactants, on both sides of the reaction surface. Moreover, a diluent is a conserved scalar and its concentration is obtained by solving a sourceless equation as well. Furthermore, by construction,

$$\sum_{k=1}^{K} Y_k = Y_f + Y_o + Y_d + Y_p = 1, \tag{11}$$

and one can determine the products mass fraction distribution from knowledge of that of the reactants and diluent mass fractions. Needless to say, not having to integrate the chemical source terms in the species transport equations, which is often stiff and forces the time step to very small values, adds to the attractiveness of this approach.

Similar treatment can be applied to obtain the temperature distribution: We combine the temperature, in the case of unity Lewis number, with the products mass fraction to formulate a second Schvab–Zeldovich variable,

$$\eta_2 = T - \frac{Q_f}{1+\varphi} Y_p, \tag{12}$$

which is governed by a transport equation of a conserved scalar similar to Eq. (9), but with different boundary conditions.

Finally, by properly normalizing all the Schvab–Zeldovich variables, and the diluent concentration, with respect to their values upstream, in their corresponding free streams, one can define a single "generic" conserved scalar,

$$s = \left(\eta_i - \eta_{i,o}\right) / \left(\eta_{i,f} - \eta_{i,o}\right), \tag{13}$$

where $\eta_{i,f}$ and $\eta_{i,o}$ are the values of η_i in the free streams carrying the fuel and oxidizer, respectively, and $i = 1, 2$ for the two variables defined by Eqs. (8) and (12). This normalized conserved scalar is governed by a sourceless convection–diffusion equation,

$$\rho \frac{\mathrm{D}s}{\mathrm{D}t} = \frac{1}{P_e} \nabla^2 s, \tag{14}$$

where $s \to 1$ in the free stream carrying the fuel species, and $s \to 0$ in the free stream carrying the oxidizer species. The solution of this single equation is sufficient to extract the distribution of all the reacting species, the reaction front location, and the temperature under condition of very fast, diffusion controlled burning. In this work, we use this limit to demonstrate the workings of the numerical algorithms. Finite-rate chemistry simulations with similar but modified algorithms have been attempted [16], and will be discussed in the context of the current algorithms in more detail in future publications.

3. Numerical algorithms

In the following we review the basic concepts in vortex and particle methods for axisymmetric flows, first for a nonreacting incompressible flow that transports a conserved scalar, then discuss their extension to low Mach number, reacting compressible flows. In the first part, the focus is on the formulation of the core function used to desingularize the vorticity and velocity associated with each element, and the evaluation of the vorticity-induced velocity field. Contrary to previous work in this area, we introduce a core function whose form depends on the location of the center of the element with respect to the symmetry line, this form is obtained conveniently from the Green function of the diffusion equation. The diffusion algorithm is then described in some detail. Diffusion plays a significant role in the evolution of flows at low and moderate Reynolds numbers (and at high Reynolds number in the close vicinity of solid walls) and, in particular, it governs the mixing rates in reacting flow. Thus, special attention is paid to the accurate simulation of the diffusion rate in this Lagrangian, grid free setting. In the second part, we discuss the impact of velocity divergence generated as the flow experience drop in density as the chemical reaction proceeds (due to the temperature rise following the exothermic heat release), and how to treat the source terms in the vorticity transport equation (which can also be extended to that of reacting scalar). The coupling of the equations through density variation is also discussed in detail.

3.1. Treatment of the incompressible vorticity field

The governing equations of vorticity transport in a constant density flow are simplified to

$$\frac{\partial \omega}{\partial t} + \left(\vec{u} \cdot \nabla\right)\omega - \frac{u}{r}\omega = \frac{1}{R_e}\left(\nabla^2 \omega - \frac{\omega}{r^2}\right) \tag{15}$$

with $\nabla \cdot \vec{u} = 0$. While there is a source term in this equation, it is actually a vorticity stretch term that vanishes in the context of a circulation-based formulation, in which the circulation associated with vortex ring elements is considered as the dependent variable.

3.1.1. Discretization and the core function

The starting point in the construction of an axisymmetric vortex method is the discretization of the continuous vorticity field among a number of computational vortex ring elements distributed within its support. In a direct simulation of a convective–diffusive process, the distance between neighboring elements is chosen to be on the order of magnitude the diffusion length scale, the smallest length in the problem, as will be shown later. In a time dependent simulation, more elements are continuously introduced to fill the gaps that form between the neighboring elements created by the convective stretch arising due to a non-uniform velocity field. More elements are also added on the outer fringes of the existing cloud of elements in order to capture the ever-expanding vorticity field due to diffusion. Alternately, the vorticity field represented by a distribution of vortex elements, having a particular core radius, can be mapped over another set of element with a different distribution and different cores. The distribution of the new element must be constructed carefully in order to satisfy some regularity requirements, and to cover the vorticity support.

A vortex element located at $\chi_i = (r_i, z_i)$ has a core radius δ_i, circulation Γ_i, and a core function [17] expressed as

$$f_{1\delta}(x, \chi_i) = \frac{1}{\delta_i^2} f_1\left(\frac{r_i}{\delta_i}, \left|\frac{z - z_i}{\delta_i}\right|, \frac{r}{\delta_i}\right). \tag{16}$$

The vorticity field is approximated by

$$\omega_\delta(x, t) = \sum_{i=1}^{N} \Gamma_i f_{1\delta}(x, \chi_i). \tag{17}$$

This approximation amounts to convolving the continuous vorticity distribution with the core function, and approximating the resulting integral using a quadrature rule. In most two (planar) and three-dimensional implementations of the vortex method, the core function is chosen to be point symmetric around its center. The latter ensures that the core function satisfies the moment condition, to some order. In this work, we use core functions that are asymmetric around the center of the core, with the asymmetry becoming more pronounced as the element approaches the centerline of the domain. Forcing the core function to depend on the location of the element center with respect to the axis of symmetry is motivated by the need to capture the asymmetry of the vorticity/velocity distribution with respect to the center of a ring element, especially when the center is close to the axis of symmetry of the flow, $r_i/\delta_i \approx \mathrm{O}(1)$. This asymmetry manifests itself most clearly very close to the centerline of the domain; where the vorticity is zero, and this condition must be satisfied numerically. The extra adaptivity gained by using asymmetric cores has been found beneficial in reducing the number of elements required to describe a given vorticity field, especially close to the centerline. The formulation also allows the core radius to vary among elements, depending on their location. Note that in the rest of the paper, ω is used to describe the discrete vorticity field, instead of ω_δ, except when equations similar to (17) are used.

The core function can be constructed using some of the kernel functions described in the literature. For reason that will become clear soon, the core function used here originates in the Green's function of the axisymmetric diffusion equation. That function describes the evolution of vorticity originally concentrated at a point, $\omega(x, x_i, 0) = \delta(r - r_i)\delta(z - z_i)$, after time t, and is given by

$$\omega(x, x_i, t) = \frac{2\pi r_i}{(4\pi\nu t)^{3/2}} I_1\left(\frac{2rr_i}{2\nu t}\right) \exp\left(-\frac{r^2 - r_i^2 + (z - z_i)^2}{2\nu t}\right), \tag{18}$$

where I_1 is the modified Bessel function of the second kind of order one. Normalized to satisfy the zero moment condition, the core function can be written in the following form

$$f_1 = \frac{2}{\left(1 - \mathrm{e}^{-r_i^2/\delta_i^2}\right)\sqrt{\pi}} \frac{r_i}{\delta_i} I_1\left(\frac{2rr_i}{\delta_i^2}\right) \exp\left(-\frac{r^2 - r_i^2 + (z - z_i)^2}{\delta_i^2}\right). \tag{19}$$

Although this core function, being asymmetric with respect to r, does not satisfy the moment conditions; it can be shown to be second order accurate [18]. This will be confirmed using the numerical results as well. Note that the core radius can be chosen as being the same for all elements, or vary slowly between elements. We should remark here that a point symmetric core function does not enforce the correct zero vorticity boundary condition at the symmetry line and does not capture the local distortion of the vorticity field near that line, nor does it enforce the correct vorticity flux there. The core function suggested here avoids these shortcomings.

3.1.2. The velocity field and convection

The vortical velocity produced by a vortex ring element is obtained by convolving the Green function of the Poisson equation in axisymmetric coordinates with the element vorticity described by the core function (see also [19,20]). The Poisson equation governing the stream function is $\nabla^2(\psi/r) = -\omega$; the stream function is defined such that the radial velocity is

$$u_\omega = -\frac{1}{r}\frac{\partial \psi}{\partial z},$$

the axial velocity is

$$v_\omega = \frac{1}{r}\frac{\partial \psi}{\partial r}.$$

The solution of this equation, written for the velocity components, is:

$$u_\omega = -\frac{\Gamma_i}{2\pi r}\int_{-\infty}^{\infty}\int_{0}^{\infty}\left(\left(z-z'\right)\frac{d_1+d_2}{d_1 d_2}\left[K(\lambda)-\left(\frac{d_1}{d_2}+\frac{d_2}{d_1}\right)\frac{E(\lambda)}{2}\right]\right) f_{1\delta}\left(r', r_i, z'-z_i\right)\mathrm{d}r'\,\mathrm{d}z', \tag{20}$$

$$v_\omega = \frac{\Gamma_i}{2\pi r}\int_{-\infty}^{\infty}\int_{0}^{\infty}\left(\left(\frac{r-r'}{d_1}+\frac{r+r'}{d_2}\right)K(\lambda)-\frac{d_1+d_2}{2}\left(\frac{r-r'}{d_1^2}+\frac{r+r'}{d_2^2}\right)E(\lambda)\right) f_{1\delta}\left(r', r_i, z'-z_i\right)\mathrm{d}r'\,\mathrm{d}z', \tag{21}$$

where

$$d_1^2 = \left(r+r'\right)^2+\left(z-z'\right)^2, \quad d_2^2 = \left(r-r'\right)^2+\left(z-z'\right)^2, \quad \lambda = \frac{d_2-d_1}{d_2+d_1},$$

K and E are, respectively, the complete elliptic integrals of the first and second kind. The double integrals in these expressions may be performed numerically during the computations, which is very costly, or the values of the double integrals can be obtained from lookup tables precomputed for given ranges of $(r-r_i)/\delta_i$, r/δ_i, and $(z-z_i)/\delta_i$. These ranges extend a distance away from the ring element center where the core function decays to very small values, $O(10^{-7})$; beyond this range, the following point vortex ring solution is applied:

$$u_\omega = -\frac{\Gamma_i}{2\pi r}\left((z-z_i)\frac{d_1+d_2}{d_1 d_2}\left[K(\lambda)-\left(\frac{d_1}{d_2}+\frac{d_2}{d_1}\right)\frac{E(\lambda)}{2}\right]\right), \tag{22}$$

$$v_\omega = \frac{\Gamma_i}{2\pi r}\left(\left(\frac{r-r_i}{d_1}+\frac{r+r_i}{d_2}\right)K(\lambda)-\frac{d_1+d_2}{2}\left(\frac{r-r_i}{d_1^2}+\frac{r+d_i}{d_2^2}\right)E(\lambda)\right) \tag{23}$$

and (r', z') are replaced with (r_i, z_i) in the definitions of (d_1, d_2). (Note that tabulated values can also be used as a time saving tool for point vortex approximation. In this case, the core radius is no longer a parameter and the dimensions of the tables are reduced making the search more computationally efficient.) Tabulation is obtained using the trapezoidal rule to compute the integrals; interpolation among neighboring values is utilized whenever necessary. Since the vorticity has been desingularized, the above integrals can also be used to evaluate the self-induced velocity of the ring element. Caution, however, must be exercised when applying this procedure to very thin elements, $\delta/r_i \leqslant 0.05$, for which very large velocities are encountered near the center of the core, requiring finer grids in evaluating the integrals. This difficulty is remedied by adding a small extra smoothing to the values of r_1^2 and r_2^2 equal to $0.56\delta^2$. The multiplier was chosen such that the self-induced velocity calculated in this approach matches its exact value (evaluated using a very fine grid).

The velocity field is used to convect the vortex ring elements, without changing their circulation. This is because

$$\Gamma = \int_A \omega \, \mathrm{d}r \, \mathrm{d}z, \quad \frac{\partial \omega}{\partial t} + (\vec{u} \cdot \nabla)\omega - \frac{u}{r}\omega = 0,$$

and the volume of the element is conserved, $\nabla \cdot \vec{u} = 0$, and hence

$$\frac{\partial \Gamma}{\partial t} + \left(\vec{u} \cdot \nabla\right)\Gamma = 0.$$

As shown in the following sections, second-order time integration is performed to convect the vortex elements, in which two velocity computations are utilized each convective time step and a second-order Euler integration method is applied to find the new location of their centers.

After few convection steps, the distance among these elements may increase if strong shear, or velocity gradient, exists, especially at high Reynolds numbers and in the neighborhood of zones of strong vorticity. In other zones, this distance may decrease continuously, due to the existence of negative strains. Without accurately redistributing the vorticity among elements, whose interdistance is carefully selected, the accuracy of the simulations deteriorates quickly [21]. This is due, in part, to the local loss of resolution, and the violation of the condition of core overlap, which must be satisfied when applying finite-core vortex methods. The process of redistributing the continuous vorticity field, which is computed from the element strength using Eq. (17), among a new set of elements or the existing set of elements supplemented with extra elements, is done during the implementation of the diffusion algorithm, which is described in the next section. A fraction of the elements may also be removed if their interdistance falls below a minimum value. Summing the circulation associated with a number of neighboring elements, and assigning the sum to a new element located at the "center of mass" of the deleted elements is one way to do this element removal.

In an incompressible flow, the velocity has two components: one generated by the vorticity, and the other is an irrotational velocity field resulting from imposing conditions at the boundaries of the computational domain, e.g., the no-flow boundary condition (in semiconfined flows) or the "free stream" velocity. The latter is not addressed in this work, as all the examples considered are flows in open domains.

3.1.3. Diffusion

In the next substep, diffusion is simulated via a modified redistribution algorithm in which vortex ring elements with finite cores are used to discretize the vorticity field. In this regard, this scheme is an extension of the work of Shankar and van Dommelon [12,13] and Shankar and Ghoniem [22] where point vortex elements were used instead of elements with finite cores [23]. Using a finite core is necessary to remove the velocity singularity in the Bio-Savart law and to provide a rational basis for interpolation between neighboring computational points. In prior implementations, a combination of desingularized vortex points for velocity calculations, singular vortex points for diffusion, and a core function to reconstruct the vorticity were used. In this work, a single core function is used for these three steps. Some of the early references to similar vorticity redistribution methods to simulate diffusion appear in Raviart [24], and the work of Rossi [25] shows other algorithms for redistributing the vorticity via diffusion. Implementation of other particle based diffusion methods in axisymmetric domains have appeared in the literature, we mention the work of Rivoalen and Huberson [11] on the particle strength exchange method [26,27] and the diffusion velocity method [28], as well as the application of a modified version of the random walk method in [10].

In the redistribution method, at each time step, the circulation of each element is redistributed amongst itself and its neighboring elements to account for the expansion of the vorticity field due to diffusion, i.e., vorticity "spilling" outside its original domain due to diffusion is captured by the neighboring elements, without changing the location of the elements. The method, therefore, is essentially explicit in time, and relies on the linearity of the diffusion equation to approximate the solution as superposition of the diffusion of all the vortex elements. A set of linear algebraic equations for the evolution of the vorticity of each element is

formulated to approximate the solution of the diffusion equation. These equations are used to determine the fraction of the vorticity to be assigned to each neighboring element following diffusion, and are obtained by matching a number of moments of the exact solution of the diffusion equation for a single element to those of the approximate solution, with the order of approximation depending on the number of matched moments. To ensure adequate resolution, the interdistance between element must of the order of magnitude of the diffusion length scale, $O(\sqrt{k\nu\Delta t})$ with $k \sim 4$. This most often requires the addition of new elements on the outer edges of the union of the existing elements. Since the presence of strong shear associated with convection near walls or in the vicinity of shear layers increases the distance between elements in the direction of maximum strain, more elements are often required within these areas. At least in an incompressible flow, this may also leads to local crowding of elements: as the distance between elements increases in the direction of extensive strains, it decreases in the perpendicular direction, and one can take advantage of this property to remove elements where they become overly crowded, i.e. where the distance is smaller than the diffusion scale. Finally elements outside the original support of vorticity must be constantly added, within the same diffusion length scale, to capture the spilling of vorticity outside its original domain. It is inevitable that the number of element in the domain will proliferate until the field becomes saturated, or unboundedly in an open domain.

To obtain the redistribution equations, recall that the element vorticity field at time t, described by

$$\omega(x,\chi_0,t) = \frac{\Gamma_0}{\left(1-\mathrm{e}^{-r_0^2/\delta_0^2}\right)}\frac{2r_0}{\sqrt{\pi}\delta_0^3} I_1\left(\frac{2rr_0}{\delta_0^2}\right)\exp\left(-\frac{r^2-r_0^2+(z-z_0)^2}{\delta_0^2}\right), \tag{24}$$

evolves according to the solution of the diffusion equation,

$$\frac{\partial\omega}{\partial t} = \nu\left(\nabla^2\omega - \frac{\omega}{r^2}\right),$$

in infinite space, to

$$\omega(x,\chi_0,t+\Delta t) = \frac{\Gamma_0}{\left(1-\mathrm{e}^{-r_0^2/\delta_0^2}\right)}\frac{2r_0}{\sqrt{\pi}\delta^3} I_1\left(\frac{2rr_0}{\delta^2}\right)\exp\left(-\frac{r-r_0^2+(z-z_0)^2}{\delta^2}\right) \tag{25}$$

after time Δt, where $\delta^2 = \delta_0^2 + 4\nu\Delta t$. We note that the circulation of the vortex ring element decays by the ratio

$$\frac{\Gamma_{\Delta t}}{\Gamma_0} = \frac{1-\mathrm{e}^{-r_0^2/\delta^2}}{1-\mathrm{e}^{-r_0^2/\delta_0^2}}$$

during the same period of time, due to diffusion across the centerline of the domain. Thus, the above equation can be written in terms of the this new circulation as

$$\omega(x,\chi_0,t+\Delta t) = \frac{\Gamma_{\Delta t}}{\left(1-\mathrm{e}^{-r_0^2/\delta^2}\right)}\frac{2r_0}{\sqrt{\pi}\delta^3} I_1\left(\frac{2rr_0}{\delta^2}\right)\exp\left(-\frac{r^2-r_0^2+(z-z_0)^2}{\delta^2}\right). \tag{26}$$

The essence of the redistribution method is to approximate the vorticity associated with an element, called here the "source" element, at $(t+\Delta t)$ and expressed by Eq. (26), using a number of elements, called here the "target" elements, composed of the same element plus a number of its neighbors using the following form

$$\omega_\delta(x,\chi_0,t+\Delta t) = \sum_{i=1}^{N_i}\Gamma_i f_{1\delta_0}(x,\chi_i), \tag{27}$$

while $\omega_\delta = \omega$ and the RHS of the last approximation is expressed by Eq. (26), N_i is the number of elements participating in the redistribution, i.e. the number of target elements, and δ_0 is the original core of the source

and target elements, if the core radius is kept the same throughout the simulations. Therefore, the redistribution process is applied to bring the core radius of the elements at $(t+\Delta t)$ back to their original value at t, while changing their strength due to diffusion. In the process of redistributing the element vorticity, the number of elements, N_i, and their locations are selected according to rules that will be described later. The core radius can be kept the same or changed, if desirable, and the same applies for the location of these elements. In either case, these locations and cores must be specified before the redistribution equations are solved.

The "redistribution" equations are obtained using the following moment condition

$$\begin{aligned}&\int_{-\infty}^{\infty}\int_{0}^{\infty}(r-r_0)^{n_1}(z-z_0)^{n_2}\omega(x,\chi_0,t+\Delta t)\,\mathrm{d}r\,\mathrm{d}z\\&\quad=\sum_{i=1}^{N_i}\int_{-\infty}^{\infty}\int_{0}^{\infty}(r-r_0)^{n_1}(z-z_0)^{n_2}\omega_i(x,\chi_i,t+\Delta t)\,\mathrm{d}r\,\mathrm{d}z\quad\text{for } 0\leqslant n_1+n_2\leqslant 2\end{aligned}\tag{28}$$

where ω_i is the "portions of the vorticity" assigned to the target elements, and $0\leqslant n_1+n_2\leqslant 2$ applies for a first-order spatial approximation, $\mathrm{O}(h)$, or alternatively, $\mathrm{O}(\sqrt{\Delta t})$. Substituting for the corresponding expressions form equations (26) and (27) and carrying out the integrals, we get the following algebraic equations governing the fractions, $b_i=\Delta\Gamma_i/\Gamma_j$, of circulation of the original element that are assigned to the target elements due to the diffusion of element j whose total circulation is Γ_j:

$$\begin{aligned}&\sum_{i=1}^{N_i}b_i=1,\\&\sum_{i=1}^{N_i}\frac{(I_0(\eta/2)+I_1(\eta/2))\mathrm{e}^{-\eta/2}r_i^2}{(1-\mathrm{e}^{-\eta})}b_i=\frac{(I_0(\mu/2)+I_1(\mu/2))\mathrm{e}^{-\mu/2}r_0^2}{(1-\mathrm{e}^{-\mu})},\\&\sum_{i=1}^{N_i}z_ib_i=z_0,\\&\sum_{i=1}^{N_i}\frac{r_i^2}{(1-\mathrm{e}^{-\eta})}b_i=\frac{r_0^2}{(1-\mathrm{e}^{-\mu})},\\&\sum_{i=1}^{N_i}\left(z_i^2+\frac{1}{2}\delta_i^2\right)b_i=\left(z_0^2+\frac{1}{2}\delta_0^2\right),\\&\sum_{i=1}^{N_i}\frac{(I_0(\eta/2)+I_1(\eta/2))\mathrm{e}^{-\eta/2}r_i^2z_i}{(1-\mathrm{e}^{-\eta})\delta_i}b_i=\frac{(I_0(\mu/2)+I_1(\mu/2))\mathrm{e}^{-\mu/2}r_0^2z_0}{(1-\mathrm{e}^{-\mu})\delta_0},\end{aligned}\tag{29}$$

where $\eta=r_i^2/\delta_i^2$ and $\mu=r_i^2/\delta_0^2$. The above equations are obtained, respectively, for the 0th moment, the r-moment, the z-moment, the r^2-moment, the z^2-moment and the rz-moment, signifying, in the same order, the conservation of circulation, mean radial and axial locations, and radial, axial and "mixed" impulse. It should be mentioned that the above equations remain valid whether the core radius of the element is kept the same or is varied. Moreover, the element core radius may be chosen as a function of location to allow for different resolutions in different zones within the domain. In such case, the above equations automatically assign the fraction of circulation, given the desired distribution of elements and their core radius.

The fact that a relatively simple analytical solution of the diffusion equation with constant coefficients is available made it possible to obtain the redistribution equations shown above by direct substitution in the moment equations (28). In general, Eq. (27) can be considered as a trial function approximation of the solution, where f_δ forms a set of known linearly independent basis functions suggested for the approximation of the solution of the diffusion equation using the trial function expressed by the summation on the left-hand side (LHS) of Eq. (27). Furthermore, the moment conditions in Eq. (28) can be viewed as a

weighted residual approximation of the differential equation, using this trail function and simple polynomial weighting functions to minimize the error resulting form the approximation, i.e. a Galerkin weighted residual approximation with weights: $w_{n_1+n_2} = r^{n_1} z^{n_2}$. While the availability of an exact solution makes it possible to simplify the analysis considerably, the same redistribution equations have been obtained using the direct Galerkin approximation for the linear diffusion equation in planar and axisymmtric geometry, and have been extended to the case of nonlinear diffusion in multi dimensions [29]. In a future article, we will demonstrate how this approach can be extended to solve yet more complex forms of the convection–diffusion–reaction equation. We also mention that this is not the approach used in the original derivation of the redistribution method in [12]; the moment-based approach presented above is analytically simpler, while the Galerkin method is more general.

The linear system of equations has N_i unknown, and must satisfy the condition that $b_i \geqslant 0$ (the positivity condition for stability, or the fact that diffusion does not change the sign of the diffusing quantity). To define that number, and the locations of the target elements, a number of elements surrounding the diffusing, or source element is selected for the redistribution process. This number is chosen within a diffusion length scale away from the source element. Since the typical distance between neighboring elements is kept within the expected spread of vorticity within a single time step, $h \sim \mathrm{O}(\sqrt{8\nu\,\Delta t})$, the neighborhood radius within which redistribution is performed is taken as $R \sim \mathrm{O}(\sqrt{16\nu\,\Delta t})$. We should mention that in all the simulations presented here, the core radius is taken as constant and equal for all elements, and $\delta \sim h$. In some cases, it is possible to limit the number of elements used in the redistribution process to six, in this case, the fractions equations in (29) can be solved directly. In other cases, it is found that more neighboring elements are required to provide for a nearly uniform distribution of computational elements within the expanding support of the vorticity, especially when the vorticity support is extending its outer boundary. In this case, $N_i \geqslant 6$, and the system of equations is solved using a simplex method. In the latter case, finding a solution for the underdetermined system while maintaining positive fractions may require adding elements in an organized fashion [13,22]. It should be noted also that elements at the outermost reach of the vorticity field whose circulation is below a certain minimum threshold may not be diffused at that time step to keep the total number of vortex elements from growing too fast. One must be careful in choosing that minimum to avoid unwarranted deterioration in accuracy.

Before closing this section, we mention that the equations become nearly singular close to the axis of symmetry (notice the dominators in Eq. (29), and special treatment is necessary to avoid numerical difficulties. Close to $r_i \to 0$, the denominators in the second, fourth and sixth equations are expanded in a Taylor series, and terms up to second order are retained. The resulting equations, which are applied for, $r < \delta$ are:

$$
\begin{aligned}
&\sum_{i=1}^{N_i} b_i = 1,\\
&\sum_{i=1}^{N_i} \left(\delta_i + \frac{C}{2}\frac{r_i^2}{\delta_i^2}\right) b_i = \delta_0 + \frac{C}{2}\frac{r_0^2}{\delta_0^2},\\
&\sum_{i=1}^{N_i} z_i b_i = z_0,\\
&\sum_{i=1}^{N_i} \left(\delta_i^2 + C r_i^2\right) b_i = \delta_0^2 + C r_0^2,\\
&\sum_{i=1}^{N_i} \left(\frac{\delta_i^2}{2} + z_i^2\right) b_i = \frac{\delta_0^2}{2} + z_0^2,\\
&\sum_{i=1}^{N_i} \left(\delta_i + \frac{C}{2}\frac{r_i^2}{\delta_i^2}\right) b_i z_i = \left(\delta_0 + \frac{C}{2}\frac{r_0^2}{\delta_0^2}\right) z_0,
\end{aligned}
\tag{30}
$$

where $C = 1/2$. While few elements fall within this zone, this treatment avoids near centerline singularities.

3.1.4. The convection–diffusion problem

Integrating the vorticity transport equation, Eq. (15), is done in two fraction steps, convection and diffusion. During the convection step, the vortex elements are transported along particle trajectories without changing their circulation, while in the diffusion step, the circulation of each element is redistributed without changing its location, while more elements may be introduced to maintain the field of computational elements well populated, and organized. In each time step, Δt, the integration of the convection–diffusion problem is split between two-half substeps, each for $\Delta t/2$. Within each half step, a convection calculation is performed. In between the two convection substeps, a diffusion calculation over the entire time step is performed. Thus, updating the element location and circulation, both denoted by the vector y, in the next set of generic equations, are obtained as follows

$$y^{t+\Delta t} = \mathfrak{I}\left(\frac{\Delta t}{2}\right)\mathfrak{R}(\Delta t)\mathfrak{I}\left(\frac{\Delta t}{2}\right)y^t, \tag{31}$$

where $\mathfrak{I}$ stands for the convection operator, and $\mathfrak{R}$ is the diffusion operator.

During each of the convection half substeps, the new element location is obtained as follows: Given $(\chi^t, \Gamma^t)_i$, $i = 1, N$, at the beginning of the time step,

(1) Calculate the velocity, $\vec{u}^t$, from Eqs. (20)–(23) for all elements.
(2) Advance the element location:

$$\chi^* = \chi^t + \vec{u}^t\frac{\Delta t}{2},$$

while keeping the circulation constant.
(3) At the new locations, calculate new values for $(\vec{u}^*)$ using Eqs. (20)–(23).
(4) Advance the element locations:

$$\chi^{t+\Delta t/2} = \chi^t + (\vec{u}^t + \vec{u}^{t*})\frac{\Delta t}{2}.$$

At the new element location, we then perform a diffusion step over Δt to update $(\chi^{t+\Delta t/2}, \Gamma^t)_i$ to $(\chi^{t+\Delta t/2}, \Gamma^{t+\Delta t})_i$. Finally steps (1)–(4) are repeated as follows; Given $(\chi^{t+\Delta t/2}, \Gamma^{t+\Delta t})_i$, $i = 1, N$,

(1) Calculate the velocity, $\vec{u}^{t+\Delta t/2}$, Eqs. (20)–(23) for all elements.
(2) Advance the element locations:

$$\chi^{**} = \chi^{t+\Delta t/2} + \vec{u}^{t+\Delta t/2}\frac{\Delta t}{2},$$

while keeping the circulation constant.
(3) At the new locations, calculate new values for $(\vec{u}^*)$ using Eqs. (20)–(23).
(4) Advance the element locations:

$$\chi^{t+\Delta t} = \chi^{t+\Delta t/2} + (\vec{u}^{t+\Delta t/2} + \vec{u}^{t**})\frac{\Delta t}{2}.$$

This concludes updating the field to $\left(\chi^{t+\Delta t}, \Gamma^{t+\Delta t}\right)_i$.

3.2. Treatment of the conserved scalar concentration field

Solving the transport equations for a conserved scalar in an incompressible flow, Eq. (14) with $\rho =$ constant, is done using a construction similar to the vortex method, although some of the details are worth reviewing. The discretization of the concentration field takes the following form

$$s_\delta(x,t) = \sum_{i=1}^{N} S_i f_{2\delta}(x,\chi_i), \tag{32}$$

where the normalized volumetric integral of the scalar concentration,

$$S_i = \frac{1}{r_i}\int_{\delta V_i} sr\,\mathrm{d}r\,\mathrm{d}z \tag{33}$$

is the conserved quantity along the particle trajectory in this case (since $\mathrm{D}s/\mathrm{D}t = 0$ and $\nabla\cdot\vec{u} = 0$ for an incompressible flow, the compressible flow case is different and will be discussed later), also called the local scalar integral. For different species mass fractions and temperature, this quantity stands for the species mass divided by the local density (the mass fraction), or the enthalpy divided by the density and specific heat (both are constant in this case). The core function takes on a slightly different form, in a way compatible with solution of the diffusion equation,

$$\frac{\partial s}{\partial t} = \frac{1}{P_r}\nabla^2 s,$$

for an initially concentrated element, namely

$$f_2 = \frac{2}{\sqrt{\pi}} I_0\left(\frac{2rr_i}{\delta_i^2}\right)\exp\left(-\frac{r^2 - r_i^2 + (z-z_i)^2}{\delta_i^2}\right); \tag{34}$$

where I_0 is the Bessel function of the first kind and zero order. The function satisfies the zero moment the condition: $\int_{-\infty}^{\infty}\int_{0}^{\infty} f_{2\delta} r\,\mathrm{d}r\,\mathrm{d}z = 1$, while

$$f_{2\delta}(x,\chi_i) = \frac{1}{\delta_i^3} f_2\left(\frac{r_i}{\delta_i}, \left|\frac{z-z_i}{\delta_i}\right|, \frac{r}{\delta_i}\right).$$

The solution of the species diffusion equation is done using redistribution equations obtained from a moment conservation expression similar to that used for vorticity,

$$\begin{aligned}\int_{-\infty}^{\infty}\int_{0}^{\infty} (r-r_0)^{n_1}(z-z_0)^{n_2} s(x,\chi_0,t+\Delta t) r\,\mathrm{d}r\,\mathrm{d}z \\ = \sum_{i=1}^{N_i}\int_{-\infty}^{\infty}\int_{0}^{\infty} (r-r_0)^{n_1}(z-z_0)^{n_2} s_i(x,\chi_i,t+\Delta t) r\,\mathrm{d}r\,\mathrm{d}z, \quad 0\leqslant n_1+n_2\leqslant 2,\end{aligned} \tag{35}$$

The resulting equations resemble those described in (29). They are, however, different in the detail due to the difference in the form of the diffusion equation and the core function:

$$
\begin{aligned}
&\sum_{i=1}^{N_i} b_i = 1,\\
&\sum_{i=1}^{N_i} \frac{\left(\left(r_i^2+\delta_i^2\right)I_0\left(\frac{r_i^2}{2\delta_i^2}\right)+r_i^2 I_1\left(\frac{r_i^2}{2\delta_i^2}\right)\right)\mathrm{e}^{-(r_i^2/2\delta_i^2)}}{\delta_i} b_i = \frac{\left(\left(r_0^2+\delta_0^2\right)I_0\left(\frac{r_0^2}{2\delta_0^2}\right)+r_0^2 I_1\left(\frac{r_0^2}{2\delta_0^2}\right)\right)\mathrm{e}^{-(r_0^2/2\delta_0^2)}}{\delta_0},\\
&\sum_{i=1}^{N_i} z_i b_i = z_0,\\
&\sum_{i=1}^{N_i} \left(r_i^2+\delta_i^2\right) b_i = \left(r_0^2+\delta_0^2\right),\\
&\sum_{i=1}^{N_i} \left(z_i^2+\frac{1}{2}\delta_i^2\right) b_i = \left(z_0^2+\frac{1}{2}\delta_0^2\right),\\
&\sum_{i=1}^{N_i} \frac{\left(\left(r_i^2+\delta_i^2\right)I_0\left(\frac{r_i^2}{2\delta_i^2}\right)+r_i^2 I_1\left(\frac{r_i^2}{2\delta_i^2}\right)\right)\mathrm{e}^{-(r_i^2/2\delta_i^2)} z_i}{\delta_i} b_i = \frac{\left(\left(r_0^2+\delta_0^2\right)I_0\left(\frac{r_0^2}{2\delta_0^2}\right)+r_0^2 I_1\left(\frac{r_0^2}{2\delta_0^2}\right)\right)\mathrm{e}^{-(r_0^2/2\delta_0^2)} z_0}{\delta_0}.
\end{aligned}
\tag{36}
$$

Near the centerline, the modified equations are obtained using similar steps to those applied previously for vorticity, and the resulting equations are the same as Eq. (30) but with $C = 1$. In the computations, the same set of elements was used to transport vorticity and scalars, and the same set of numerical parameters, e.g., $\Delta\tau$ and δ, was chosen for both solutions. The redistribution, however, followed equations (29) for vorticity and (36) for scalars.

3.2.1. The convection–diffusion problem

Similar to the integration of the vorticity transport equation, the integration of the conserved scalar transport equation, Eq. (14), is done in two fraction steps, convection and diffusion, and hence will not be repeated here in detail. However, if the same elements are used to transport vorticity (circulation) and scalar concentration (scalar integrals), then there is no need to repeat the convection steps, and only diffusion, or the redistribution of the scalar integrals, is performed between the two convection half steps to update $(\chi^{t+\Delta t/2}, S^t)_i$ to $(\chi^{t+\Delta t/2}, S^{t+\Delta t})_i$. This constitutes a substantial saving in computational time.

A final note regarding the scalar transport calculations is concerned with computing the scalar gradients whose value is required in the vorticity source term. This gradient is obtained by differentiating the core function of the scalars, i.e.

$$
(\nabla s)_\delta(x,t) = \sum_{i=1}^{N} S_i \nabla f_{2\delta}(x,\chi_i). \tag{37}
$$

Other approaches to obtain the gradients in grid free simulation have been suggested (see, e.g. [20]), we use the above equation for simplicity and comment on its accuracy in the discussion of the results. Differentiation the core function imposes more stringent requirement on the uniformity of the element distribution and the interelement distance, and results will be shown to demonstrate the accuracy for different choices.

3.3. Treatment of the reacting field

Reacting flows are characterized by temporally and spatially variable density field, which changes the formulation and the numerical schemes in a fundamental way. The vorticity transport equation of a reacting flow, Eq. (7), contains two extra terms beyond the convection–diffusion equation analyzed so far, connected with the spatial changes in the flow density (a kinematic effect), and the interaction between the

density gradient and the material acceleration (baroclinic effect). Like in the case of incompressible flow, this equation is solved in fraction steps: convection, diffusion and generation, the latter involves the integration of the source term. Generation is the most complex process since it requires the evaluation of the spatial density gradients and the redistribution of the updated circulation among the elements, every time step. Moreover, the continuity equation, in this case, Eq. (1), includes an extra term related to the temporal changes in the density, leading to a finite velocity divergence. The velocity divergence introduces an extra velocity component. The density is obtained from the equation of state, and its gradients are evaluated by differentiating that equation, which depends on the spatial gradients of the chemical species and the temperature. These latter quantities are determined from the solution of the conserved scalar variable defined in the Formulation section. Meanwhile, both temporal and spatial gradients of the density affect the species transport equation itself. The treatment of each of these terms is described next individually, and then the overall scheme is presented.

3.3.1. Convection and diffusion

The convective and kinematics terms, on the RHS of Eq. (7),

$$\frac{\partial\omega}{\partial t} + (\vec{u}\cdot\nabla)\omega - \left(\frac{u}{r} - \nabla\cdot\vec{u}\right)\omega = 0,$$

after integration over a material elemental area, δA, lead to the statement of the well-known Kelvin–Helmholtz theorem for a variable density flow: $\mathrm{D}\Gamma/\mathrm{D}t = 0$. Written for the discrete vorticity field, we have: $\mathrm{D}\Gamma_i/\mathrm{D}t = 0$ for each vortex element for which $\mathrm{d}\chi_i/\mathrm{d}t = \vec{u}(\chi_i(t))$, confirming the fact that in a variable-density flow, in the absence of source terms whose treatment is described next, the circulation remains constant along particle trajectories. Thus, except for the expansion-induced velocity due to the temporal change in density, which is discussed later in this section, convection is treated in the same way as in the incompressible case.

Diffusion, the second term on the LHS, is simulated using the redistribution algorithm described above, assuming that locally the density varies weakly, that is, in constructing the distribution equation, the local density of the element being diffused is used (consistent with neglecting the variation of the diffusivity with temperature).

3.3.2. The baroclinic source term

The first term on the RHS of Eq. (7), the source term,

$$\dot{\Omega} = -\frac{1}{\rho}\left(a_z\frac{\partial\rho}{\partial r} - a_r\frac{\partial\rho}{\partial z}\right) \tag{38}$$

is treated in another fractional step, following convection, as follows. Given the density gradients and the material acceleration at the end of the convection step, the baroclinic source terms are computed, and the objective is to update the circulation of each element according to the integration of the source term over the area element, $\mathrm{d}\omega/\mathrm{d}t = \dot{\Omega}(\vec{r})$. Using the discrete form of the vorticity distribution in Eq. (17), and applying a first-order forward integration, we get

$$\sum_{j=1}^{N} f_{1\delta}(x,\chi_j)\,\Delta\Gamma_j = \dot{\Omega}(x)\,\Delta t. \tag{39}$$

This equation is applied to all elements, i.e. for $x = \chi_i, i = 1, N$, leading to N equations in the fractional change of the local circulation at the centers of the vortex elements, $\Delta\Gamma_j = \Gamma_j(t+\Delta t) - \Gamma_j(t)$, due to the source term;

$$\sum_{j=1}^{N} f_{1\delta}(\chi_i,\chi_j)\,\Delta\Gamma_j = \dot{\Omega}(\chi_i)\,\Delta t. \tag{40}$$

Note that the RHS is not the fractional change of the circulation of the individual elements, but the cumulative change at the element center due to all the elements. To find the former, $\Delta\Gamma_j$, we must solve this linear system, whose coefficient matrix (the interpolation matrix) is ill conditioned. To overcome this difficulty, we use the following iterative scheme suggested in [30]

$$\Delta\Gamma_j^{(m+1)} = \frac{\dot{\Omega}(\chi_j)\Delta t - \sum_{i\in P(j)} f_{1\delta}(\chi_j,\chi_i)\Delta\Gamma_i^{(m)}}{\sum_{i\in Q(j)} f_{1\delta}(\chi_j,\chi_i)}; \quad j = 1-N, \tag{41}$$

where $Q(j)$ contains the set of elements which are within a small distance d^* from element j, $P(j)$ is its complement, and m is the iteration number. In the simulations we used $d^* \sim \delta$, and convergence to 10^{-6} was achieved within $m \sim 5$–8, even for very large N. The same steps can be repeated to derive a second-order time integration algorithm for the source terms in the vorticity transport equation.

3.3.3. The density and its gradient

Evaluating the baroclinic source term,

$$-\frac{1}{\rho}\left(a_z\frac{\partial\rho}{\partial r} - a_r\frac{\partial\rho}{\partial z}\right),$$

requires knowledge of the density and it gradients at the location of the elements. This must be done with some care since the density is obtained from the equation of state;

$$\rho = \frac{1}{T\sum_{k=1}^{K} Y_k/W_k}, \tag{42}$$

and hence its derivative must be evaluated using the following expression;

$$\nabla\rho = -\rho\frac{\nabla T}{T} + \frac{\sum_{k=1}^{K}\nabla Y_k/W_k}{T\sum_{k=1}^{K} Y_k/W_k}. \tag{43}$$

The species concentrations and the temperature are computed from the distribution of the conserved scalar, s, which is computed from the most recent values of the scalar integral, S_i. Updating the latter will be described soon, for now it suffices to state that once $s(x,t)$ is known, then the corresponding Schvab–Zeldovich variables, $\eta_1 = \eta_{1,o} + (\eta_{1,f} - \eta_{1,o})s$ and $\eta_2 = \eta_{2,o} + (\eta_{2,f} - \eta_{2,o})s$ are evaluated, and the location of the reaction front $r_F = r_F(z,t)$ is determined from, $\eta_1(r_F,z,t) = 0$. On one side of the reaction front, we have $Y_o = \eta_1$ and $Y_f = 0$, while on the other side, $Y_f = -\eta_1/\varphi$ and $Y_o = 0$. The diluent concentration is obtained form; $Y_d = Y_{d,o} + (Y_{d,f} - Y_{d,o})s$, and the products concentration is $Y_p = 1 - (Y_o + Y_f + Y_d)$. The temperature is obtained form the second variable:

$$\eta_2 = \eta_{2,o} + (\eta_{2,f} - \eta_{2,o})s \quad \text{and} \quad T = \eta_2 + \frac{Q_f}{1+\varphi}Y_p.$$

Updating the scalar integral is described in detail in the following section.

Eq. (37) is used to determine the gradients of T and Y_k using the definitions of the conserved scalars in Eqs. (8) and (11): e.g., $\nabla\eta_1 = (\eta_{1,f} - \eta_{1,o})\nabla s$, where $\nabla\eta_1 = \nabla Y_o - \varphi\nabla Y_f$ and hence: $\nabla Y_o = \nabla\eta_1$ and $\nabla Y_f = 0$ on the oxidizer side of the reaction front, while $\nabla Y_f = -\nabla\eta_1/\varphi$ and $\nabla Y_o = 0$ on the fuel side, and $\nabla Y_p = -\left(\nabla Y_o + \nabla Y_f + \nabla Y_d\right)$. The temperature gradient is obtained similarly from the second Shvab-Zeldovich variable, Eq. (12), where

$$\nabla\eta_2 = (\eta_{2,f} - \eta_{2,o})\nabla s \quad \text{and} \quad \nabla T = \nabla\eta_2 + \frac{Q_f}{1+\varphi}\nabla Y_p.$$

Thus, having updated the conserved scalar, one can evaluate its derivatives and those of all the chemical species and temperature, and substitute in the equation above to evaluate the density gradient. Finally the particle acceleration is computed as the material derivative along particle trajectories following a convection step over time step, Δt_c, e.g. for the radial direction

$$\frac{\mathrm{D}a_r}{\mathrm{D}t} \approx \frac{u\big(\chi_j(t+\Delta t_c), t+\Delta t_c\big) - u\big(\chi_j(t), t\big)}{\Delta t_c}. \tag{44}$$

3.3.4. The scalar field

Now we discuss the integration of the scalar transport equations for a reacting flow. Note that the source term for a chemical species transport equation is obtained from the variable density form of that equation

$$\rho\left[\frac{\partial s}{\partial t} + \Big(\nabla\cdot\vec{u}\Big)s + s\Big(\nabla\cdot\vec{u}\Big)\right] = \frac{1}{P_r}\nabla^2 s + \rho s\Big(\nabla\cdot\vec{u}\Big). \tag{45}$$

The LHS,

$$\rho\left[\frac{\partial s}{\partial t} + \Big(\nabla\cdot\vec{u}\Big)s + s\Big(\nabla\cdot\vec{u}\Big)\right] = 0$$

represents the impact of convective transport on the scalar distribution in a compressible field, and shows that: $\mathrm{D}S_i/\mathrm{D}t = 0$, where S_i is the local volume integral of s over the ring element defined in Eq. (33). Note that the scalar integral used in the variable density case is the same as the one used in the constant density case; the convective derivative, however, is different due to the finite velocity divergence in the former case. The first term on the RHS of Eq. (45) represents the contribution of diffusion, and the second term represents the local source term and is modified using the continuity equation, such that

$$\frac{\partial s}{\partial t} = \frac{-s}{\rho}\left(\frac{\mathrm{D}\rho}{\mathrm{D}t}\right) = \Psi. \tag{46}$$

The changes in the local value of s due to the source term are computed using a similar algorithm to that introduced above for handling the changes in the element vorticity, i.e.; writing

$$\sum_{j=1}^{N} f_{2\delta}(x_i, \chi_j)\,\Delta S_j = \Psi(x_i)\,\Delta t, \tag{47}$$

where ΔS_j is the change of the element strength due to the source term, $\Delta S_j = S_j(t+\Delta t) - S_j(t)$. Solving this system of equations using the same algorithm described by Eqs. (40) and (41) yields the incremental changes and the new values of the strength of the elements, or local scalar integrals, due to the source term. Evaluating the source term in Eq. (46) requires the material derivative of the density along the particle trajectory, which is done following a convection step using the approximation

$$\frac{\mathrm{D}\rho}{\mathrm{D}t} \approx \frac{\rho\big(\chi_j(t+\Delta t_c), t+\Delta t_c\big) - \rho\big(\chi_j(t), t\big)}{\Delta t_c}. \tag{48}$$

Here we mention again that the density is computed using the equation of state, after the chemical species and temperature distributions have been updated.

3.3.5. The expansion velocity

In the case of a reacting flow, the density varies due to the exothermic heat release, and at low Mach number, this variation is confined to zones where the chemical reaction active. In this case, the continuity equation shows that the velocity field has finite divergence where the density changes along particle trajectories, given by

$$\nabla \cdot \vec{u} = -\frac{1}{\rho}\frac{\mathrm{D}\rho}{\mathrm{D}t} = \varepsilon. \tag{49}$$

For the purpose of introducing the effect of this divergence, the total velocity

$$\vec{u} = \vec{u}_\omega + \vec{u}_e \tag{50}$$

is decomposed into a vorticity induced velocity, $\vec{u}_\omega$, and an expansion induced component, $\vec{u}_e$, which is evaluated such that its divergence satisfies Eq. (49). Towards this end, the Lagrangian derivative of the density of the elements are computed following the generation step using Eq. (48), to evaluate ε, and these values are then applied to calculate resulting local divergence strength, E_i using the following equation

$$\varepsilon \approx \varepsilon_\delta(x_i, t) = \sum_{i=1}^{N} E_i f_{2\delta}(x_i, \chi_i). \tag{51}$$

With the expansion velocity determined from a velocity potential ϕ, such that: $u_e = \partial\phi/\partial r$ and $v_e = \partial\phi/\partial z$, the solution of the resulting Poisson equation, $\nabla^2\phi = \varepsilon$, is obtained in a way similar to that used to obtain the vorticity induced velocity, that is, far from the element center, the field is approximated as a point source ring, while close to the ring center, the velocity field is given by:

$$\begin{aligned} u_e &= \sum_{i=1}^{N} \frac{E_i}{2\pi r}\int_{-\infty}^{\infty}\int_{0}^{\infty}\left\{\left(\frac{r-r'}{d_1}-\frac{r+r'}{d_2}\right)K(\lambda)\right. \\ &\quad \left.+\frac{d_1+d_2}{2}\left(\frac{r+r'}{d_2^2}-\frac{r-r'}{d_1^2}\right)E(\lambda)\right\} f_{2\delta}(r', r_i, z'-z_i)\,\mathrm{d}r'\,\mathrm{d}z', \\ v_e &= \sum_{i=1}^{N} \frac{2E_i}{\pi}\int_{-\infty}^{\infty}\int_{0}^{\infty}\left\{\frac{r'(z-z')}{d_1 d_2}\left[\frac{1}{d_1+d_2}K(\lambda)+\frac{1}{2}\frac{d_1+d_2}{d_1 d_2}E(\lambda)\right]\right\} f_{2\delta}(r', r_i, z'-z_i)\,\mathrm{d}r'\,\mathrm{d}z'. \end{aligned} \tag{52}$$

The definitions of the symbols are as before. The integrals are evaluated numerically and tabulated for later use (see discussion above).

3.4. The convection–diffusion–generation problem

During each time step, the vorticity transport equation, Eq. (7), and the conserved scalar equation, Eq. (14), are integrated simultaneously to update the circulation and conserved scalar integral. The circulation and scalar integral are then used to calculate the velocity, species concentrations and temperature, while the equation of state, Eq. (42) is used to update the density (note that the continuity equation, Eq. (1), is applied to impose the velocity divergence due to combustion). Similar to the solution of the convection–diffusion problem for incompressible flow, in which fractional steps are used to account for the impact of each operator separately, in combustion (convection–diffusion–generation), multiple substeps are performed every integration time step as follows.

Each time step, Δt, the integration of the convection–diffusion–generation problem is split between two-half substeps, each for $\Delta t/2$ within which a convection–generation integration is performed, and a diffusion

integration over the entire time step is performed in between. Thus, updating the element circulation and scalar integral, all denoted by the vector y in the next set of generic equations, are obtained as follows

$$y^{t+\Delta t} = \mathfrak{I}^*\left(\frac{\Delta t}{2}\right)\mathfrak{R}(\Delta t)\mathfrak{I}^*\left(\frac{\Delta t}{2}\right)y^t; \tag{53}$$

where, $\mathfrak{I}^*$ stands for the convection–generation operator, and $\mathfrak{R}$ is the diffusion operator.

During each of the convection–generation half substeps, the element location, circulation, and scalar integral, are obtained using a predictor–corrector scheme as follows: Given their values at the beginning of the time step; $(\chi^t, \Gamma^t, S^t)_i$, $i = 1, N$:

(1) Calculate the velocity, $\vec{u}^t$, Eqs. (20)–(23) and (52), scalar concentration, s^t, equation, species concentration, Y_k^t, temperature, T^t, and density, ρ^t, equation, for all elements.
(2) Advance the element locations:

$$\chi^* = \chi^t + \vec{u}^t\frac{\Delta t}{2},$$

while keeping the circulation and scalar integral constant.
(3) At the new locations, calculate new values $\left(\vec{u}^*, s^*, Y_k^*, T^*, \rho^*, \nabla\rho^*\right)$.
(4) Calculate the material derivatives:

$$\left(\frac{\mathrm{D}\vec{u}}{\mathrm{D}t}\right)^* \approx \frac{\vec{u}^* - \vec{u}^t}{\Delta t/2} \quad \text{and} \quad \left(\frac{\mathrm{D}\rho}{\mathrm{D}t}\right)^* \approx \frac{\rho^* - \rho^t}{\Delta t/2}.$$

(5) Update the element circulation and scalar integral using the source terms, $\dot{\Omega}^*$, Ψ^*, calculated from Eqs. (38) and (46), respectively, on the basis of the latest values of

$$\left((\nabla\rho)^*, \left(\frac{\mathrm{D}\vec{u}}{\mathrm{D}t}\right)^*, \left(\frac{\mathrm{D}\rho}{\mathrm{D}t}\right)^*\right)$$

to get (Γ^*, S^*) using Eqs. (40) and (47) over a $\Delta t/2$.
(6) Given $(\chi^{t^*}, \Gamma^{t^*}, S^{t^*})_i$, $i = 1, N$, calculate a new velocity, $\vec{u}^{t*}$.
(7) Advance the element locations:

$$\chi^{t+\Delta t/2} = \chi^t + (\vec{u}^t + \vec{u}^{t^*})\frac{\Delta t}{2}.$$

(8) At the new locations, calculate new values $(s^{t^*}, Y_k^{t^*}, T^{t^*}, \rho^{t^*}, \nabla\rho^{t^*})$.
(9) Calculate the average material derivatives:

$$\frac{\mathrm{D}\vec{u}^{t^*}}{\mathrm{D}t} \approx \frac{1}{2}\left(\frac{\vec{u}^* - \vec{u}^t}{\Delta t/2} + \frac{\vec{u}^{t^*} - \vec{u}^t}{\Delta t/2}\right) \quad \text{and} \quad \frac{\mathrm{D}\rho^{t^*}}{\mathrm{D}t} \approx \frac{1}{2}\left(\frac{\rho^* - \rho^t}{\Delta t/2} + \frac{\rho^{t^*} - \rho^t}{\Delta t/2}\right).$$

(10) Update the element circulation and scalar integral using source terms $\dot{\Omega}^*$, Ψ^*, based on the latest values of

$$\left(\nabla\rho, \frac{\mathrm{D}\vec{u}}{\mathrm{D}t}, \frac{\mathrm{D}\rho}{\mathrm{D}t}\right)^{t^*}$$

to get $(\Gamma^{t+\Delta t/2}, S^{t+\Delta t/2})$.

(11) Now, we have $(\chi^{t+\Delta t/2}, \Gamma^{t+\Delta t/2}, S^{t+\Delta t/2})_i$, $i = 1, N$.

Next vorticity and scalar are diffused over the entire time step, without moving the elements to update $(\chi^{t+\Delta t/2}, \Gamma^{t+\Delta t/2}, S^{t+\Delta t/2})_i$ to $(\chi^{t+\Delta t/2}, \Gamma^{t+\Delta t^*}, S^{t+\Delta t*})_i$. The convection–generation calculations, steps (1)–(11), are then repeated in the same way as in the first half substep to complete the time step to obtain $(\chi^{t+\Delta t}, \Gamma^{t+\Delta t}, S^{t+\Delta t})_i$.

4. Numerical results

Numerical results that demonstrate the convergence characteristics of the diffusion and the diffusion–convection algorithms are presented first, followed by a similar study for the combustion problem. The primary objective here is to examine the accuracy and the convergence rate of the algorithms by comparing the results to those obtained analytically, from numerical solutions using other methods, or simply by refining the numerical parameters to reach converged solutions. Of particular importance is the dependence of the accuracy on the different numerical parameters, namely the time step, that also determines the average interelement distance in the redistribution method, and the core radius of the elements. In all cases, the vortex ring problem, in different incarnations, is used. We start with the solution of the diffusion problem, for which an exact solution exists, and evaluate the error for different choices for the time step, or the element inter distance since they are dependent, the core radius and the overlap ratio. As expected, the latter plays a very important role. Next, the coupled convection–diffusion problem is solved, and the results are compared with an accurate finite-difference solution for the propagation of a vortex ring at relatively low Reynolds number. Here we focus on the impact of the overlap ratio, which emerges as one of the most important parameters, on the error. Finally, the reacting ring problem, that is a fuel ring in an oxidizer atmosphere, is solved and the impact of the time step, for a fixed overlap ratio, on the accuracy is examined.

4.1. The diffusion problem

We solve the vorticity and scalar diffusion equations;

$$\frac{\partial \omega}{\partial t} = \frac{1}{R_e}\left(\nabla^2 \omega - \frac{\omega}{r^2}\right) \quad \text{and} \quad \frac{\partial s}{\partial t} = \frac{1}{P_r}\nabla^2 s,$$

respectively, for the evolution of a concentrated vortex ring initially at $r_0 = 1$ and $z_0 = 0$. The initial circulation is scaled such that $\Gamma_0 = 1$, and the viscosity is scaled to yield a Reynolds number $R_e = \Gamma_0/\nu = 50$. Similar initial conditions are used for scalar diffusion, the initial distribution is given by $s(x, 0) = \delta(r - 1)\delta(z)$, with a unit mass of the diffusing scalar, and equal values for the Peclet number and the Reynolds number. (Note that while the scalar diffusion problem is physically realistic when the densities of the diffusing mass and the bulk are the same, it is not so for the vorticity diffusion case since vorticity generates a velocity field in which it is convected. Nevertheless we use this idealization to examine the accuracy of the diffusion algorithm). Both diffusion problems have analytical solutions, which are used as benchmarks. The boundary conditions are: zero vorticity and scalar concentration at infinity, zero vorticity along the axis of symmetry and zero radial scalar gradients there. Note also that, besides the extra term in the vorticity diffusion equation, the different boundary conditions lead to different distributions for these two quantities.

The formulation of the numerical algorithms indicates that there are two numerical parameters that determine the temporal and spatial resolution of the method: the time step and the core radius. The core function defined above, which can be thought of as a Gaussian core modified is such a way that it adjusts to the axisymmetric geometry of the domain, is not second order in the classical sense since it is asymmetric

around the core center. However, given that the asymmetry is confined to a small region close to the axis, it is expected that, for sufficiently resolved distribution, the convergence rate should approach second order. On the other hand, the number of conserved moments in the redistribution method was chosen to yield a scheme that is limited to a first-order spatial accuracy (given that the distribution of the elements is not particularly organized) and hence the overall convergence rate may not be second order.

The following results are shown to illustrate the impact of the time step, given in terms of $\Delta\tau = v\,\Delta t$ or the average distance between the elements, $h = \sqrt{8\Delta\tau}$, the core size and the overlap ratio, δ/h, independently, by varying one while fixing all the others, over a wide range. The numerical results are compared with the exact solution of the diffusion equation using the L2 norm of the errors in the vorticity and scalar concentration, computed over a uniform grid covering nonzero values of both. The norms of the error are evaluated at $\tau = 0.2$.

In the first set of results, the core radius was kept constant, $\delta = 3\sqrt{8\Delta\tau^*}$ with $\Delta\tau^* = 0.0005$, while the time step was varied $0.00025 \leqslant \Delta \leqslant \tau \leqslant 0.1$. Increasing $\Delta\tau$ has the effect of reducing the resolution and, since the core radius was kept constant, also reducing the overlap ratio. Results in Fig. 1, plotted as function of the distance among the elements, h, shows that the error increases as $O((h)^{2.2})$. As mentioned above, by conserving six moments in the redistribution method while using neighboring elements distributed arbitrarily within the diffusion length scale, we were able to derive a first-order spatial approximation of the diffusion equation. On the other hand, the numerical result shows a second-order spatial approximation! This should not be totally unexpected since the loss of one order of accuracy in the discretization leading to the moment equations can be related to the nonuniform distribution of elements in the vicinity of the diffusing element [29]. Given that a uniform grid is never imposed on the solution, one should not presume that "mesh" uniformity is achievable (as in a typical finite difference scheme). Nevertheless, in the numerical

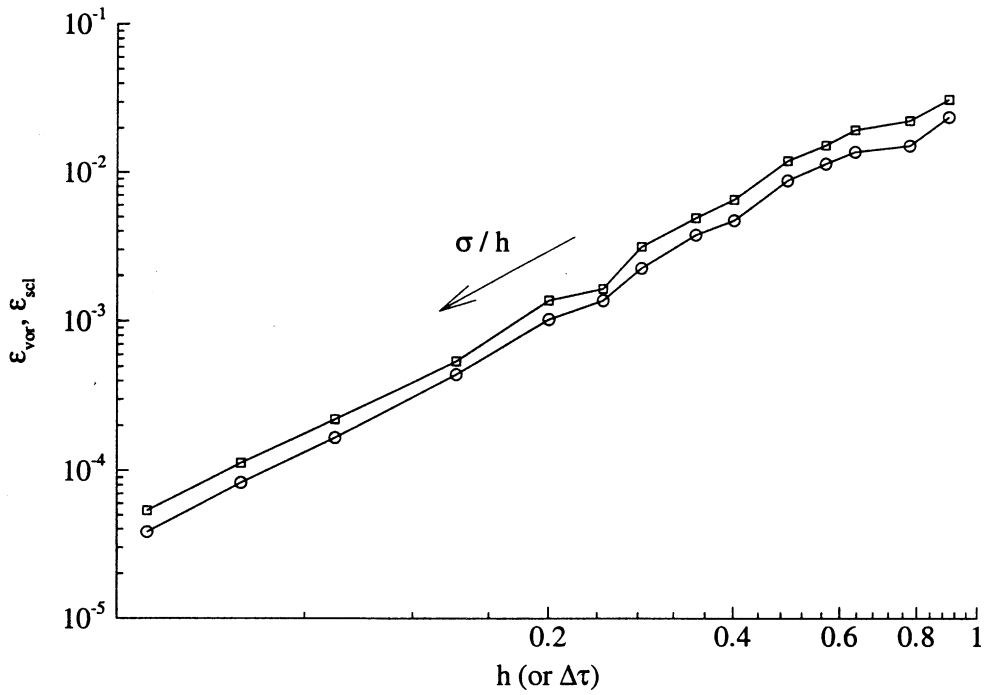

Fig. 1. Solution of the diffusion equation, using a vortex ring as a model problem. Impact of the time step or interelement distance for a fixed core size. Circles correspond to the vorticity and squares to the scalar concentration.

solution, elements are continuously added in the neighborhood of each diffusing element, in an orderly fashion, whenever necessary, i.e. whenever gaps arise between the elements. Numerical results show that this leads to an approximately uniform distribution of elements, i.e. the order of the numerical solution approaches that obtained on a uniform distribution of elements. As expected, the number of elements grows as the resolution is refined. This is shown in Fig. 2, where the number of elements increases almost linearly as h is reduced.

In another set of numerical experiments, the time step, and hence the average distance between the elements was kept constant, $\Delta\tau = 0.0005$, while the overlap was varied while keeping the core radius larger than the element interdistance, $1 \leqslant \delta/h \leqslant 10$. Results in Fig. 3 show that the error decreases at a second-order rate, $O((\delta)^{2.1})$. Here again we observe second-order convergence, confirming that the choice of the core function, although asymmetric, leads a second-order discretization (we suspect that the core function, being itself local solution of the diffusion equation, should lead to second-order truncation, a mathematical proof is needed to support this statement). It is interesting that the error continues to decrease as the overlap ratio increases within the range of parameters attempted here! In the meantime, fixing the overlap ratio, by varying the core as the time step, or h, changes, leads to very small change in the error, as depicted in Fig. 4. These results were obtained for an overlap ratio of 2.

Results presented so far can be combined to show that the error in the redistribution approximation of the diffusion equation, using the modified Gaussian core and a number of moments corresponding to a first-order spatial discretization but with careful selection of the location of the inserted elements is $O((\delta/h)^2)$. Finally Fig. 5 shows a comparison between the numerical vorticity contours and their exact counter part for different values of the time step and the core size. It is clear that strong overlap is necessary to maintain high accuracy.

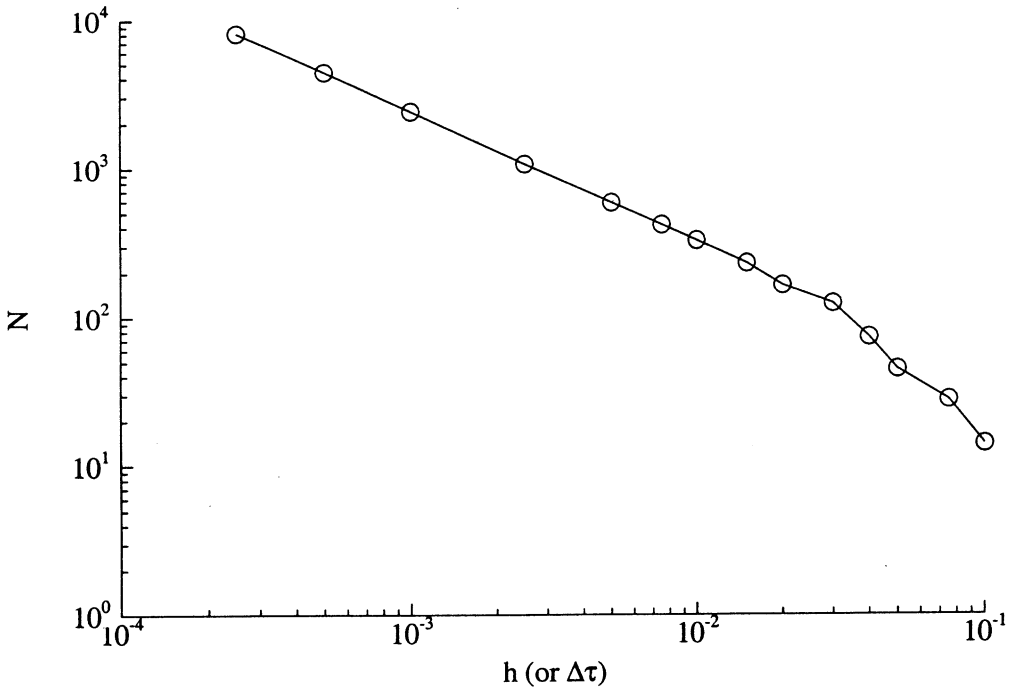

Fig. 2. The impact of the time step or the interdistance between neighboring elements on the total number of vortex element at the last time step of the simulation. Similar to the results in Fig. 1, the core radius is held constant.

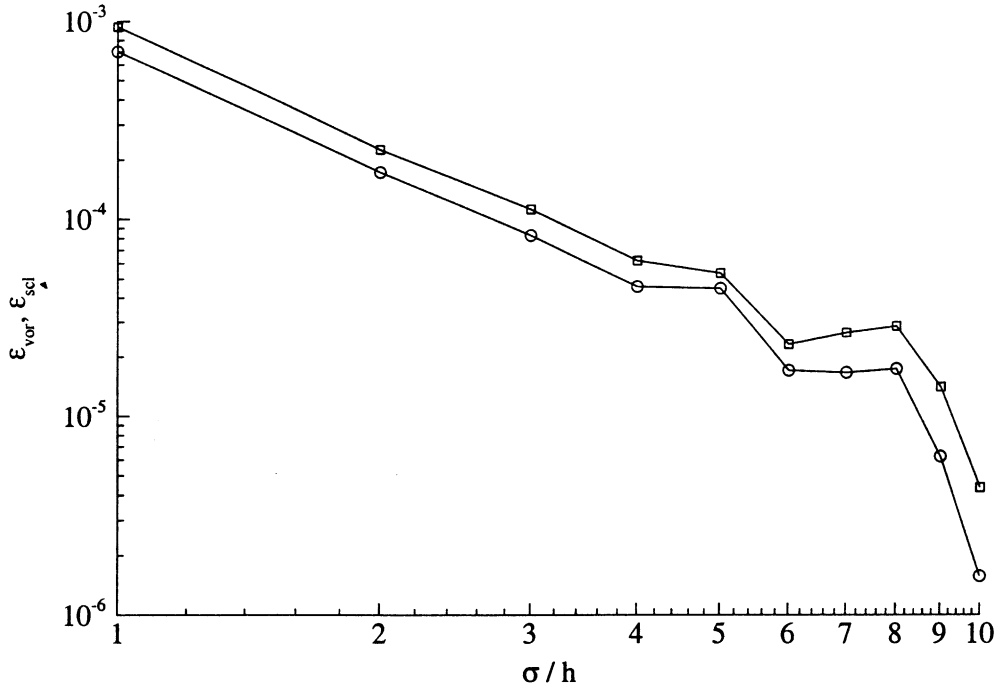

Fig. 3. Solution of the diffusion equation, using a vortex ring as a model problem. The impact of the overlap ratio on the error in the vorticity, shown in circles, and the scalar concentration, shown by the squares, for a fixed time step or interdistance between elements, at the final step of the calculation.

4.2. The convection–diffusion problem

The next set of numerical data is obtained for a propagating vortex ring, i.e. we solve the incompressible, unsteady, Navier–Stokes equation, starting with a very thin vortex ring. At $t=0$, the center of the ring is located at (1,0), the initial circulation is unity and the Reynolds number is 50. The initial conditions are desingularized by working with diffusion alone for few time steps, while neglecting the impact of convection, until the concentrated ring spreads over a very small radius around its original location. This propagating vortex ring problem does not have an exact solution and we use an accurate finite-difference solution for comparison [18]. Here again we study the impact of the numerical parameters on the errors, noting that the errors resulting form convection, diffusion and fractional step integration of the two processes (or operators). We will focus on the errors in the vorticity solution with some reference to that in the scalar propagation.

First, Fig. 6 shows the evolution of the computational points for a case with $\Delta\tau = 0.0005$ and $\delta/h = 2$. Note the higher concentration of elements around the initial center of the ring, and their tendency to "multiply" faster around the downstream side of the propagating ring where more of the vorticity tends to migrate. Also, due to the nature of scalar diffusion (the zero gradient at the centerline), higher concentration of elements are observed near the symmetry line, between it and the original center of the ring. Note also the overall asymmetric distribution of the elements with respect to the center. At the final time step, the total circulation of the ring is almost 70% of its initial value due to vorticity diffusion and cancellation across the centerline. During this period, the number of elements has grown from 415 to 5720 to accommodate the expanding ring. The total mass of the conserved scalar is constant, by construction. The figure shows that the computational elements spread adaptively over the region of nonzero vorticity, covering a

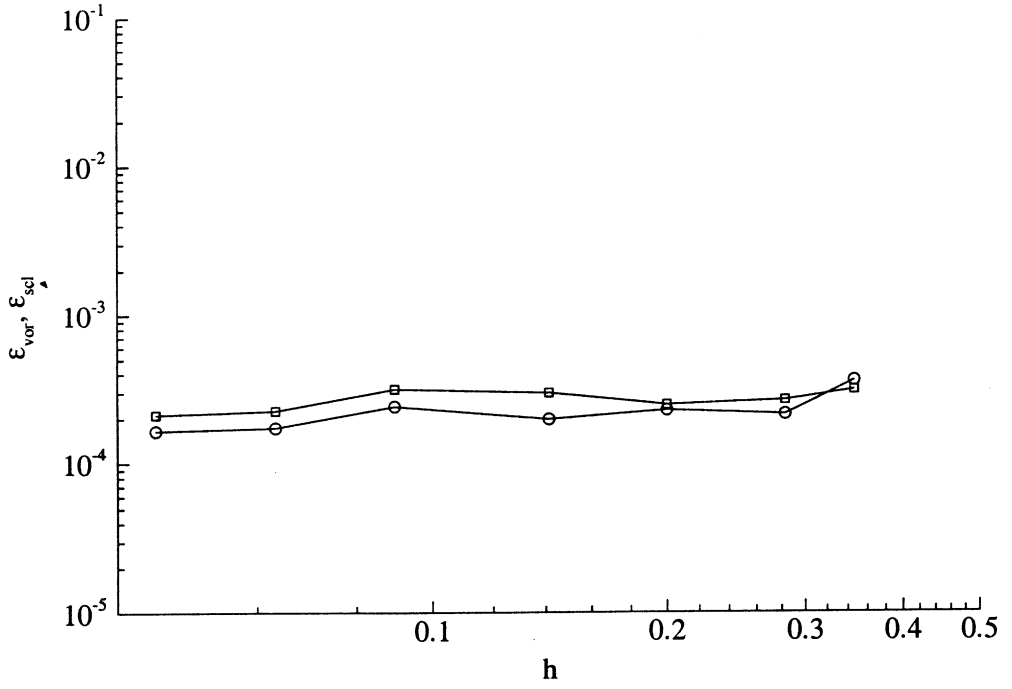

Fig. 4. Solution of the diffusion equation, using a vortex ring as a model problem. The impact of the time step or interdistance between elements on the error in the vorticity, shown in circles, and the scalar concentration, shown by the squares, for a fixed overlap ratio, at the final step of the calculation.

zone which expands in time following the spread of the vorticity via diffusion. Higher concentration of vorticity near the center of the expanding ring corresponds to higher element number density near the initial center of the ring. The zone of nonzero vorticity is covered almost uniformly with elements, i.e. no holes are observed in the computational grid. The two small concentric circles shown in the last figure illustrate the typical separation between the elements, represented by the inner circle, and the core radius, depicted by the outer circle. The corresponding vorticity and scalar concentration distributions are shown in Fig. 7, in gray scale and line contours, respectively. Note that the vorticity decays to zero along the axis of symmetry, while the scalar maintain zero gradient, leading to the separation of the centers of vorticity and scalar concentration.

The accuracy of the results is now discussed by comparing the vortex solution with the finite-difference solution, considering the latter as a benchmark solution. One measure of the numerical error is that encountered in the impulse of the vortex ring, defined as $I_{\omega r} = \sum_{i=1}^{N} \Gamma_i r_i^2$, and expected to remain zero as the ring propagates. Fig. 8 shows that the impulse for $\Delta\tau = 0.002,\ 0.001\, and\, 0.0005$ is approximately 7, 3, and 1×10^{-5}, all measured at $\tau = 0.2$, for the same value of the overlap parameter $\delta/h = 2$. It is important to mention that the number of elements used at the last time step of the simulation increases from 1688 to 3069 to 5720 as the time step was reduced. With finer resolution, the growth of the error with time is substantially reduced. The axial expansion of the ring, $I_{\omega z} = \sum_{i=1}^{N} \Gamma_i z_i^2$, shows that the vortex solutions track the finite difference solution very closely for all the cases tested here. The L2 of the vorticity errors were also computed for the same case, and the values obtained were 3.91, 2.63, and 1.82×10^{-4}, showing almost linear dependence on the time step, that is second-order dependence on the interdistance between the particles, when the core overlap is maintained constant.

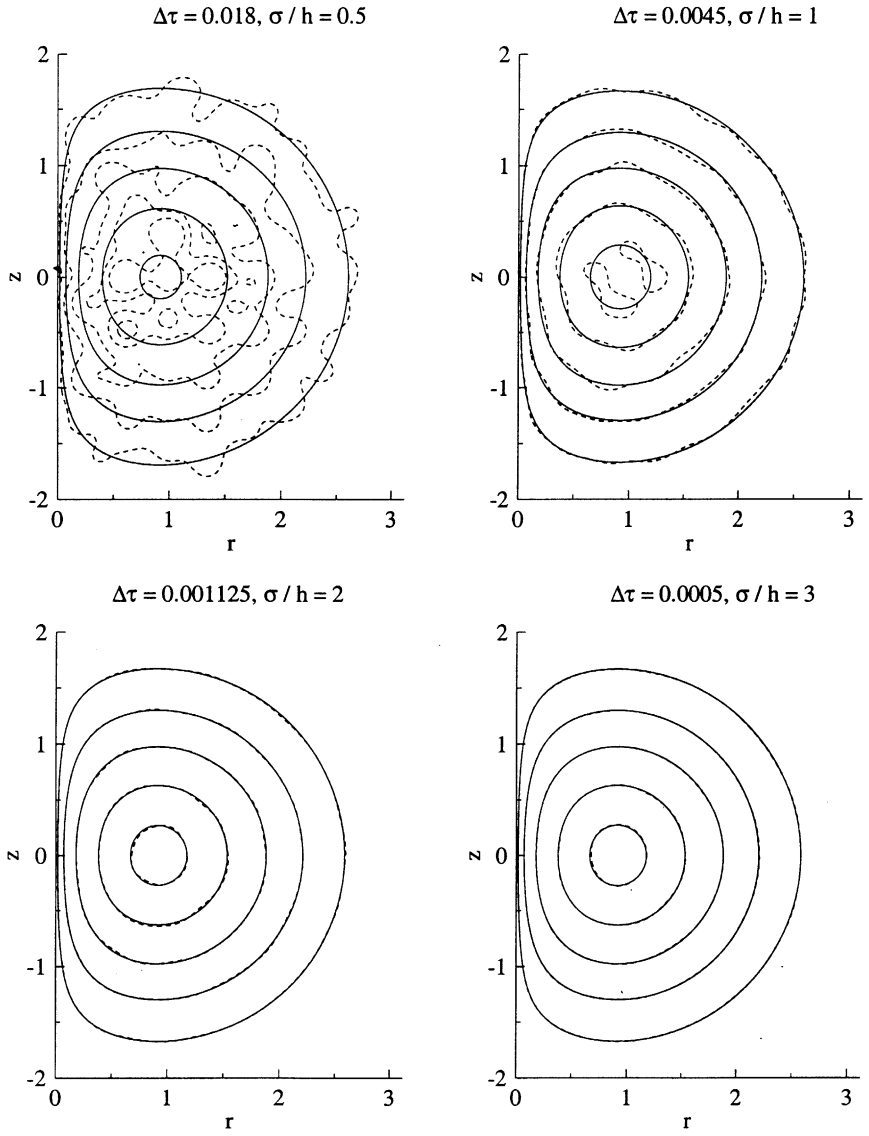

Fig. 5. Solution of the diffusion equation, using a vortex ring as a model problem. Comparison between the exact solution of the diffusion equation, shown in solid lines, and the numerical solution, shown in broken line, for the case or a diffusing vortex ring. Results are shown in terms of the vorticity contours, corresponding to vorticity 0.01, 0.04, 0.2, and 0.3, all evaluated at the same time, $t = 0.2$. Results are obtained using the same core radius but different integration time steps, leading to different overlap ratios, as shown.

The impact of the time step for a fixed core size is more complicated, as shown in Fig. 9 for $0.01 \geqslant \Delta\tau \geqslant 0.0005$ and $\delta = 0.245$. Decreasing the time step lowers the error to a point, beyond which it appears that other factors and/or sources become important and that the combined effect is to keep the error constant! Decreasing the time step, or h, at constant core also has the effect of increasing the overlap ratio, which has been shown in the solution of the diffusion problem to have a strong impact on the discretization error. However while in the solution of the diffusion equation, larger overlap always led to lower

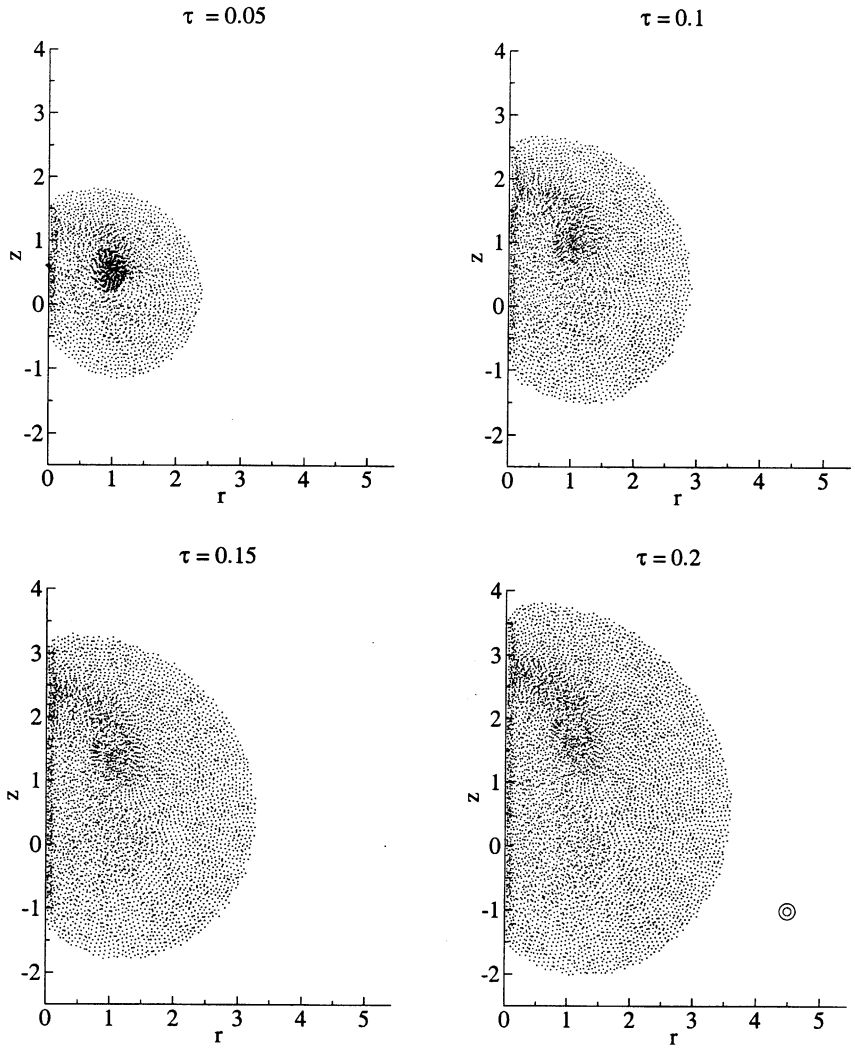

Fig. 6. Solution of the convection–diffusion equation, using a vortex ring as a model problem. The figure shows the computational points used to discretized the vorticity field at different times, for overlap ratio of 2 and time step of 0.0005. The number grows from 415 at the initial step to 5720 at the final step. The two small concentric circles correspond to the element interdistance and the core radius.

errors, in this convection–diffusion problem, there seems to be an optimum value for the overlap, beyond which increasing overlaps contributes positively to the error. This is despite the fact that in this algorithm, there is also a fractional step error, which decreases with smaller values of the time step.

Another set of experiments was conducted for fixed overlap ratio while increasing the core radius, i.e., both the time step and the core radius were allowed to change together. Results shown in Fig. 10 indicate that the error increases with the interdistance/core radius monotonically in this case. These two sets of results show that the error drops as the overlap rises (by increasing the core or decreasing the distance between elements), while it rises with the core radius, suggesting that trends similar to those predicting in the inviscid analysis, in which the total error was shown to be a superposition of a discretization error that depends of the core radius and a

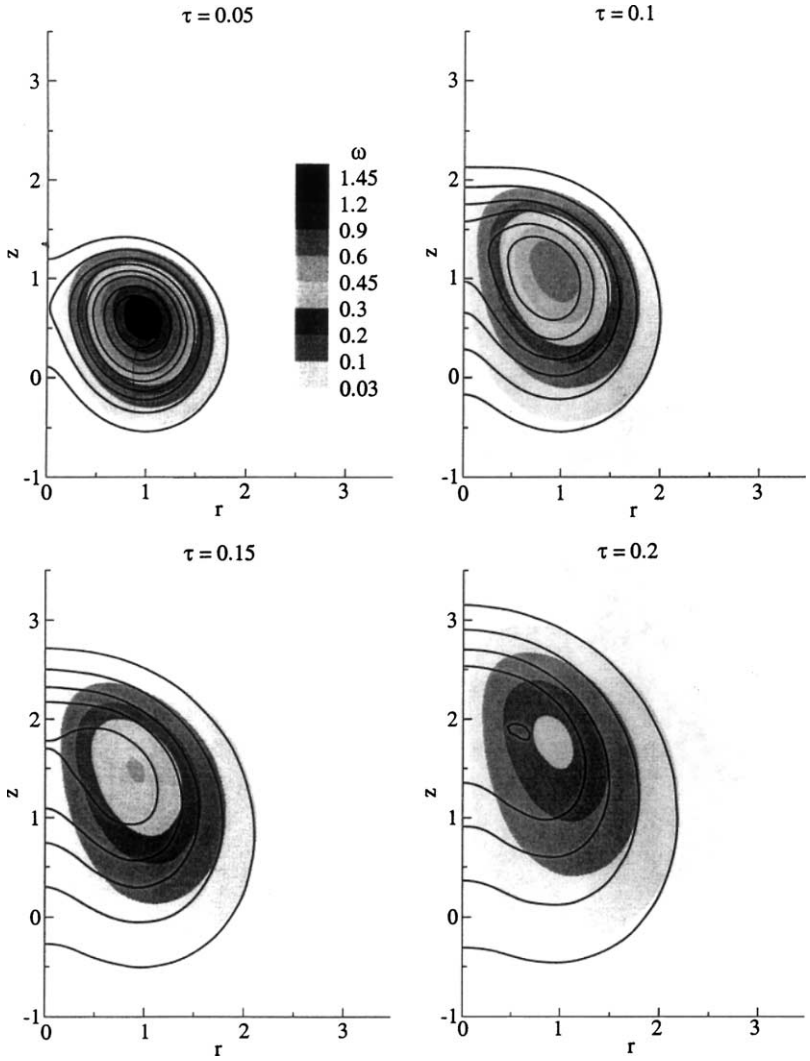

Fig. 7. Scalar concentration, shown by line contours, and the vorticity, shown in zones of gray, for the problem described in this figure. Scalar concentration contours correspond to values of 0.03, 0.1, 0.2, 0.3, 0.45, 0.6, 0.9, 1.2, and 1.45. The gray scale for vorticity is shown on the side.

smoothing error which depends on both the overlap ratio and the core radius. Of course, the numerical results presented here are for Navier–Stokes equations and include a viscous simulation error and a splitting error as well, contrary to those derived in the theoretical results for the inviscid flow.

Finally, Fig. 11 shows results obtained for the same propagating vortex ring problem using a fixed value for h, while increasing the core size such that $1.0 \leqslant \delta/h \leqslant 3.535$. Clearly, there is an optimal value for the element core overlap beyond which the errors rise towards values similar to those encountered when computing with small cores. Numerical experiments show that this value for normalized core overlap is close to 2. Similar trends have been observed in other vortex simulations, and predicted by analysis of inviscid methods. The results seem to agree with the proposition that the error has two components that can be expressed as: $\delta^n + (h/\delta)^l \delta^2$, where the first, "smoothing" error depends solely on the choice of the order of the core function and the core radius, while the second, "discretization" error depends on the overlap

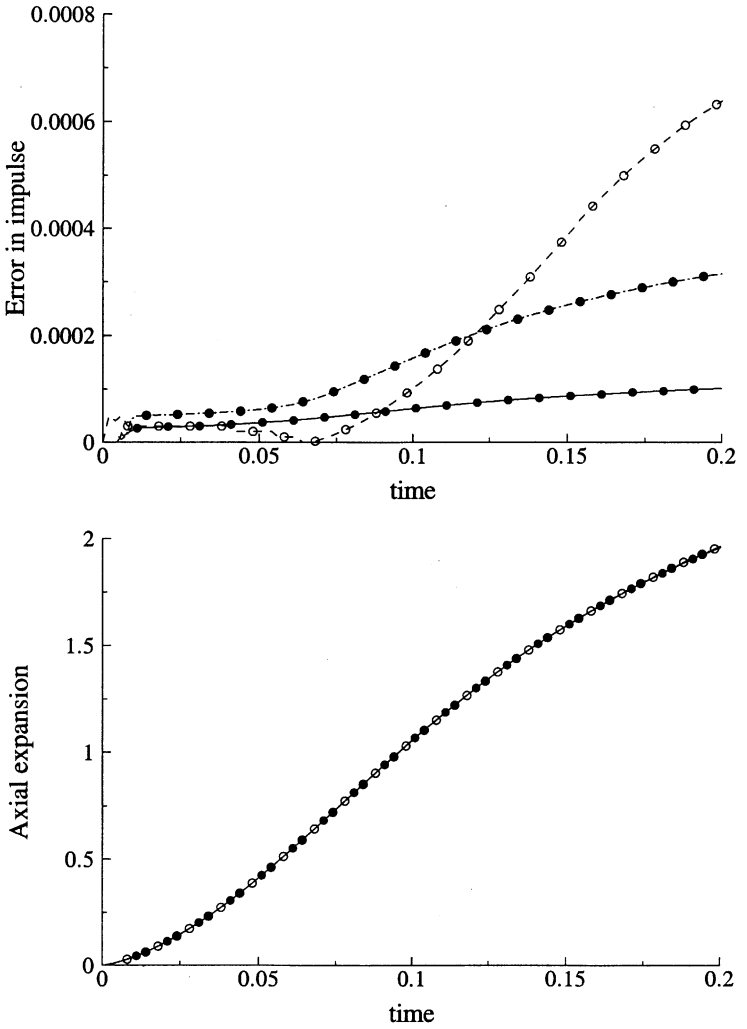

Fig. 8. The impact of the time step on the error in the solution of the convection diffusion problem, described in Fig. 7 and this figure, shown in terms of the error in the axial impulse in the top figure and a comparison between the axial expansion of the vortex ring, computed using the vortex element method, and an accurate finite difference solution, shown in the lower figure. The open circle corresponds to time step on 0.002, gray circle to 0.001 and black circle to 0.0005. The line in the lower figure is the finite difference solution. Results are obtained for a fixed core overlap ratio.

ratio and the core radius, with n and $l > 1$. Fixing the core radius of the elements, with larger than unity overlap, while changing the interdistance between the elements reduces the overall error until the smoothing error becomes dominant. On the other hand, fixing the interdistance while varying the core radius decreases the overall error until the smoothing error dominates. Finally, fixing the overlap ratio, the overall error changes monotonically with the core radius.

The impact of this overlap on the error is a shown in Fig. 12 where vorticity, shown at top, and scalar concentration contours, shown at bottom, at the last time step of the simulations are depicted for different values of the overlap ratio, and compared with the finite difference solution. Weak overlap leads to an oscillatory solution, while strong overlap leads to a diffuse solution, in agreement with the designation of the error terms discussed above. Overall, the accuracy of the solution with $\sigma/h = 2$ is good.

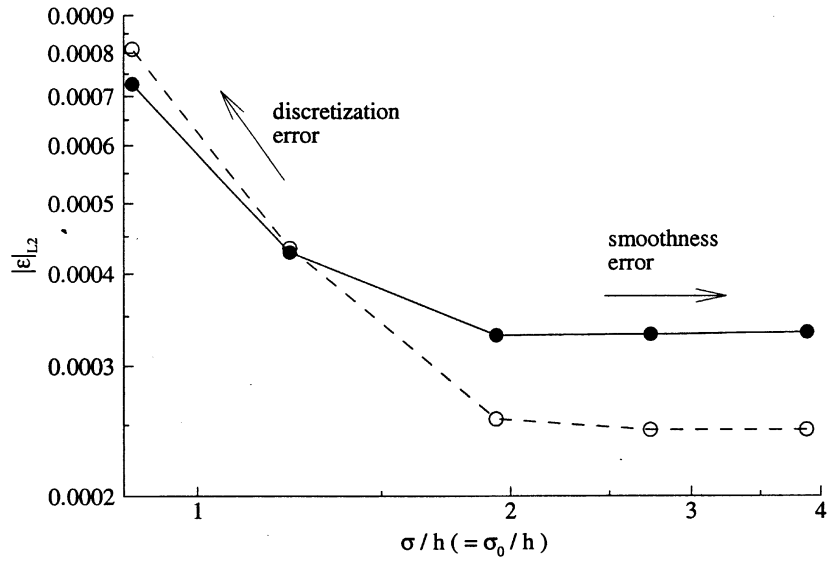

Fig. 9. Impact of the time step on the vorticity error, shown in dark circles, and scalar concentration, shown in open circles, evaluated for a fixed core size and shown in terms of an inverse of the interelement distance, for time steps $0.01 > \Delta\tau > 0.005$ and $\delta = 0.245$.

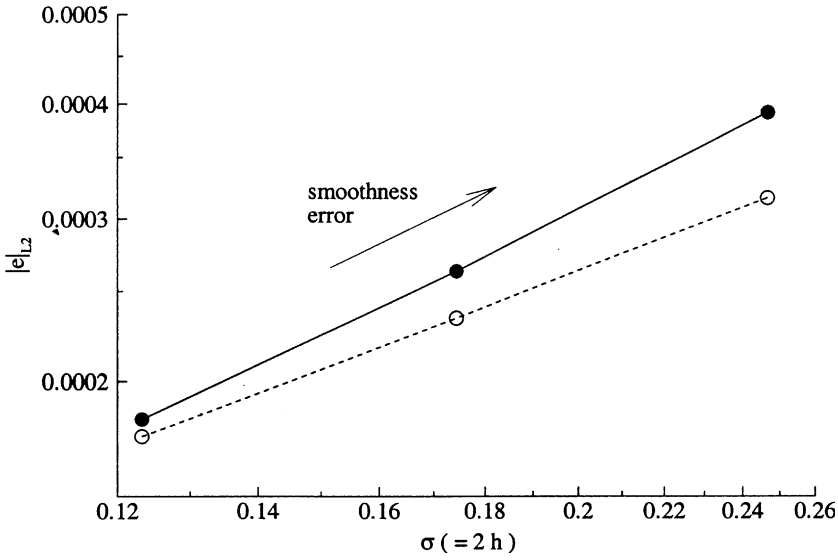

Fig. 10. Impact of the core size, evaluated for a fixed overlap ratio (i.e., both the interelement distance and core vary), on the vorticity (dark circles) and concentration (open circles) errors for the problem shown in Fig. 8. Overlap ratio is held at 2.

4.3. The combustion problem

The combustion algorithm, in which an extra velocity component arising due to the volumetric expansion associated with the heat release, and the source terms in the vorticity transport equation and the scalar transport equation are finite, was implemented to simulate the burning of a fuel element. Initially, the fuel element is shaped in the form of a diffuse ring in a surrounding oxidizing environment. (In the laboratory,

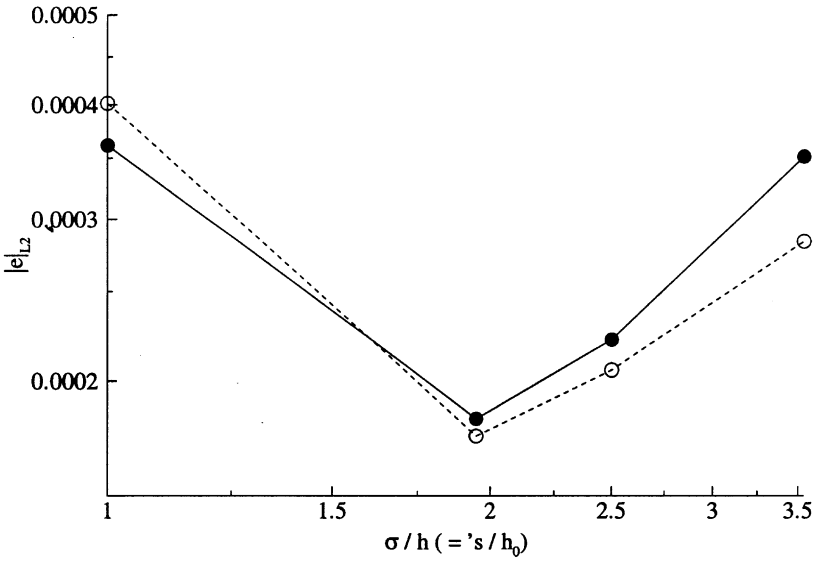

Fig. 11. The dependence of the vorticity (dark circles) and scalar concentration (open circles) errors on the overlap ratio for a fixed value of the interelement distance, $\Delta\tau = 0.0005$.

this fuel ring could be generated using a periodically pulsed fuel jet in stagnant air, as the jet accelerates into air, it partially diffuses into the entrained air to form a ring whose core is made of pure fuel while its outer shell is a mixture of fuel and air. If the jet is slow enough, the initial vorticity in the ring can be neglected with respect to the buoyancy-generated vorticity that forms later). The initial velocity of the fuel and surrounding air is taken to be zero, and the flow is only generated by buoyancy as high temperature products form at the boundary between fuel and air due to diffusive mixing followed by reaction.

The fuel has the properties of methane, CH_4, and the stoichiometric chemical reaction corresponding to complete combustion of the hydrogen, H_2, and carbon, C, is

$$CH_4 + 2(O_2 + 3.76N_2) \rightarrow CO_2 + 2H_2O + 7.52N_2.$$

The molecular weights of different species are: for methane, $M_f = 16$, for oxygen, O_2, $M_o = 32$, for nitrogen, N_2, $M_d = 28$, and for the products mixture, $CO_2 + 2H_2O$, $M_p = 26.62$ (average molecular weight for water and carbon monoxide). Other physical parameters required for the simulations are: the mass stoichiometry $\varphi = 4$, the normalized enthalpy of reaction is $Q_f = 80$, and the Reynolds number is $R_e = 50$, based on the initial radius of the core of the fuel ring. The center of the ring is located at (1,0). The initial conditions are as follows:

On the fuel side, that is near the center of the ring, the concentrations and temperature are: $Y_f = 1, \quad Y_o = 0, \quad Y_p = 0, \quad Y_d = 0, \quad T = 1.$

On the air side, far from the ring center, the concentrations and temperature are: $Y_f = 0, \quad Y_o = 0.2, \quad Y_p = 0, \quad Y_d = 0.8, \quad T = 1.$

The initial conditions were obtained in a way consistent with the diffusion equations as follows. For a short period of time at the beginning of the simulations and until $\tau_0 = 0.002$, only diffusion (and reaction for the reacting species) was allowed to spread an initially concentrated fuel element into air, i.e. the weak impact of convection was neglected. At the end of this period, the spreading element was represented using 756 computational elements, whose spatial distribution is shown in Fig. 13, and the corresponding profiles of the different chemical species are shown in Fig. 14. At this moment, the fuel and other species

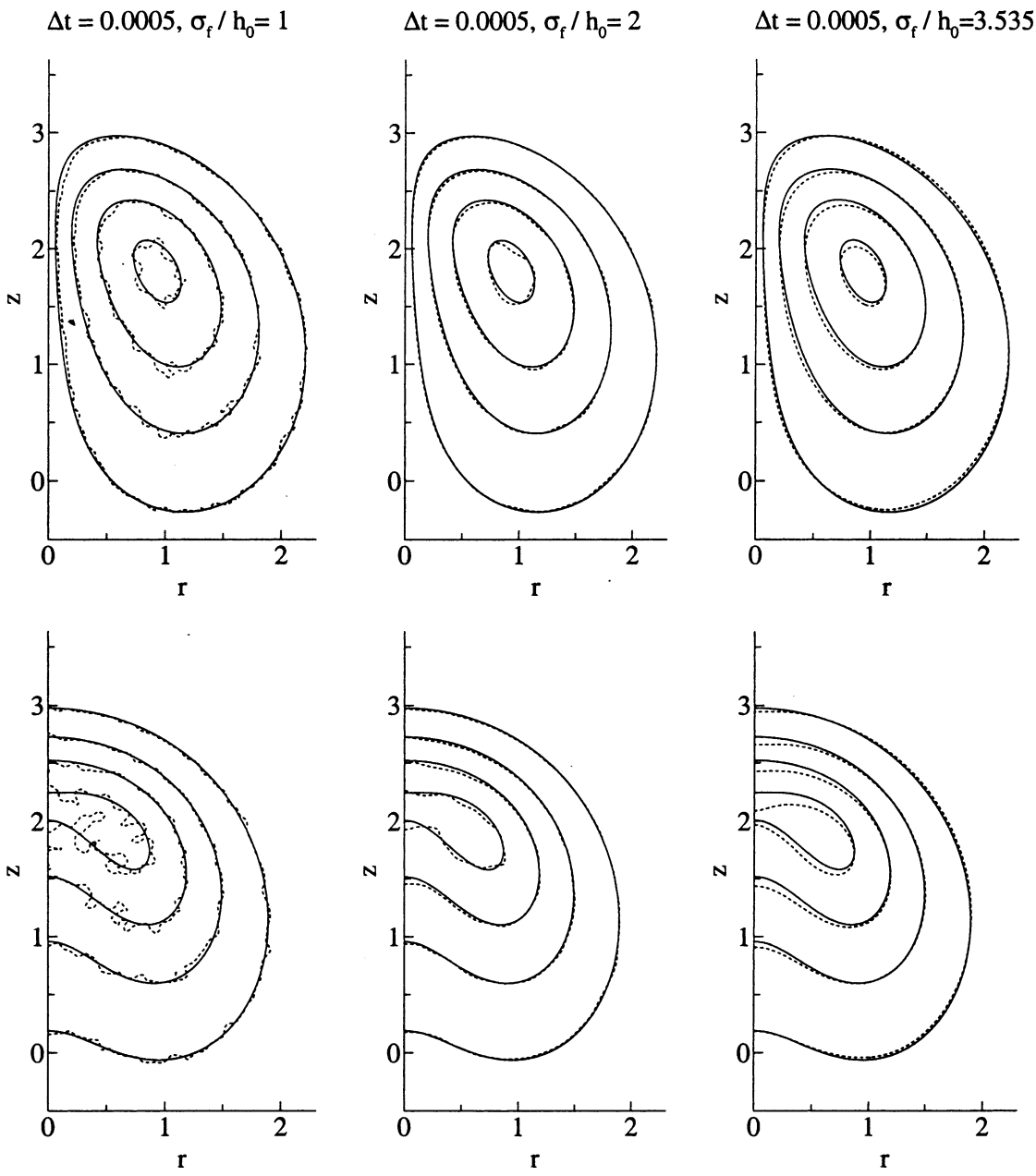

Fig. 12. The vorticity contours shown in the top figure and the scalar concentration contours shown in the lower figure for different values of the overlap ratio, all for the same time step, and compared with an accurate finite difference solution, shown in continuous lines.

concentration are rescaled such that the fuel concentration at the center of the fuel puff is unity. No vorticity generation or convection is allowed during this period. This exercise is meant to produce the initial conditions for the combustion calculation presented next.

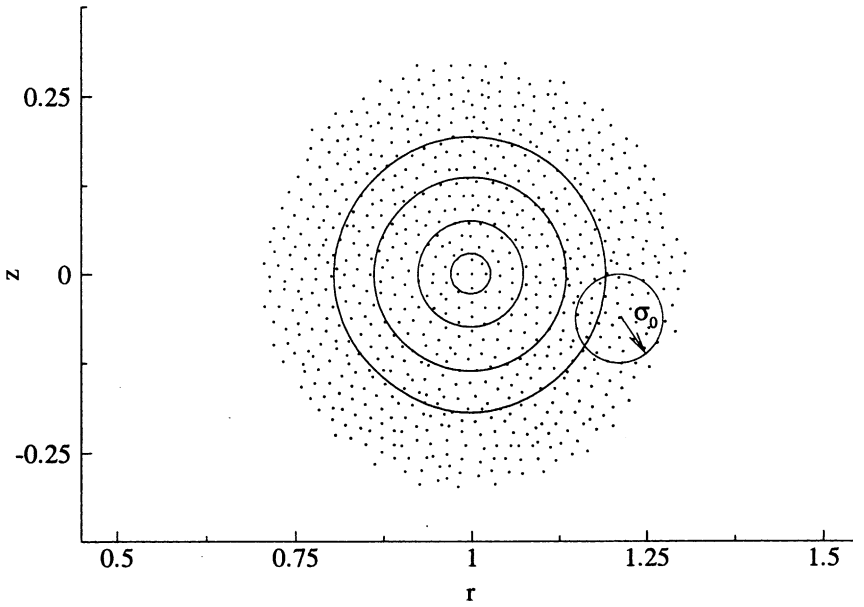

Fig. 13. The initial distribution of elements used to capture the initial conditions of the reacting ring problem. The contours show the distribution of the mixture fraction, whose values are 0.01, 0.1, 0.5, and 0.9. The small circle shows the core size of the element.

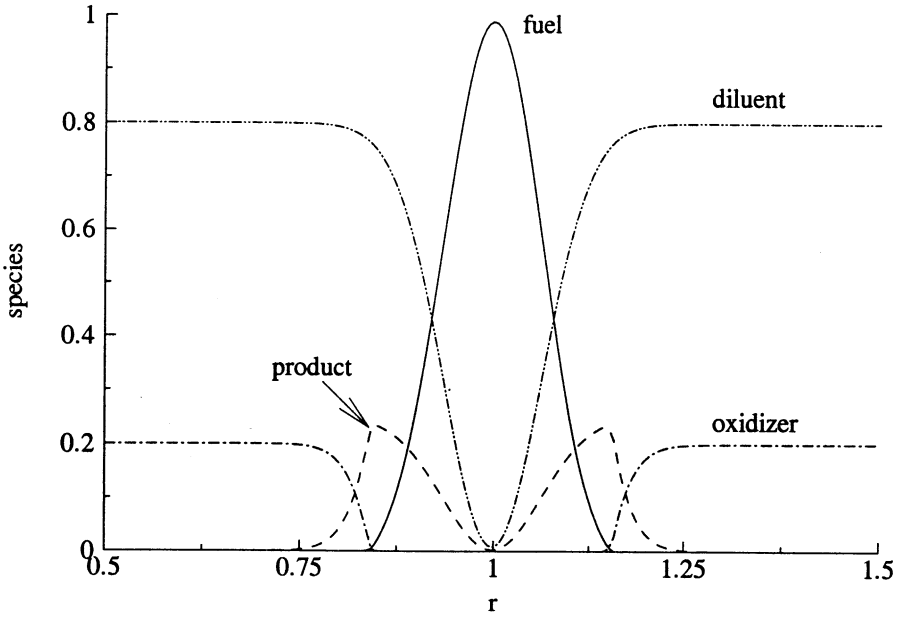

Fig. 14. The initial distribution of the fuel, oxidizer, product and diluent concentrations for the reacting ring problem.

Combustion simulations were obtained for the following values for the time steps: $\Delta\tau = v\Delta t = 0.0005$, 0.001, 0.002 and 0.005, to examine the convergence rate as a function of the time step and the interelement distance. In all cases, the relation between the distance between the elements and the time step was kept as $h = \sqrt{8\Delta\tau}$. The core radius was fixed as twice the inter element distance, $\sigma = 2h$. In the following, results of

the simulation are shown in terms of the vorticity, fuel concentration and temperature, and the figures are used to define the different stages of evolution of this flow in which the tight coupling between the flow dynamics and the diffusion of the chemical species is demonstrated. Results obtained at the smallest time step are used in the following discussions. Next, we discuss we analyze the dependence of the results on the numerical parameters to define the convergence rate.

Fig. 15 shows the temperature distribution and the vorticity at the early stages of the simulations, at $\tau = 0.005$, the former on a gray scale and the latter as solid and broken contour lines. Since the original center of the fuel ring is at a larger distance from the centerline than its core radius, there is very weak interaction with the centerline, and the early stages of the solution resembles that of a pair of vortex rings in the planar case. The temperature distribution is symmetric around the center of the core as the fuel diffuses outwards and burns to form products. Note also that since the initial vorticity is zero everywhere, convection has a weak impact on the temperature distribution. Vorticity is generated through the interaction between gravity and the radial density gradients, essentially preserving the initial symmetry around the core center at the early stages, with almost perfect symmetry around the vertical axis of the core. This development leads to the formation of what can be characterized as two nascent vortex rings (each with a core in the shape of a semicircle), the vorticity of the inner ring is negative, while that of the outer ring is positive. Consistent with the zero initial vorticity of the ring, its center has moved very little in the vertical direction, i.e., there is a delay between the start of the diffusion and the formation of sufficient vorticity, which then propels the ring.

As time evolves, more vorticity is generated, and diffusion spreads the reacting fuel core towards the axis of symmetry as well as outwards in the radial direction. Diffusion across the axis of symmetry weakens the inner ring, and the onset of asymmetry is observed by time $\tau = 0.05$, as shown in Fig. 16. Further evolution of the flow demonstrates the persistence of the two-ring structure, and the dominance of the outer vortex ring, as the overall structure spins in the clockwise direction while it rises. The almost

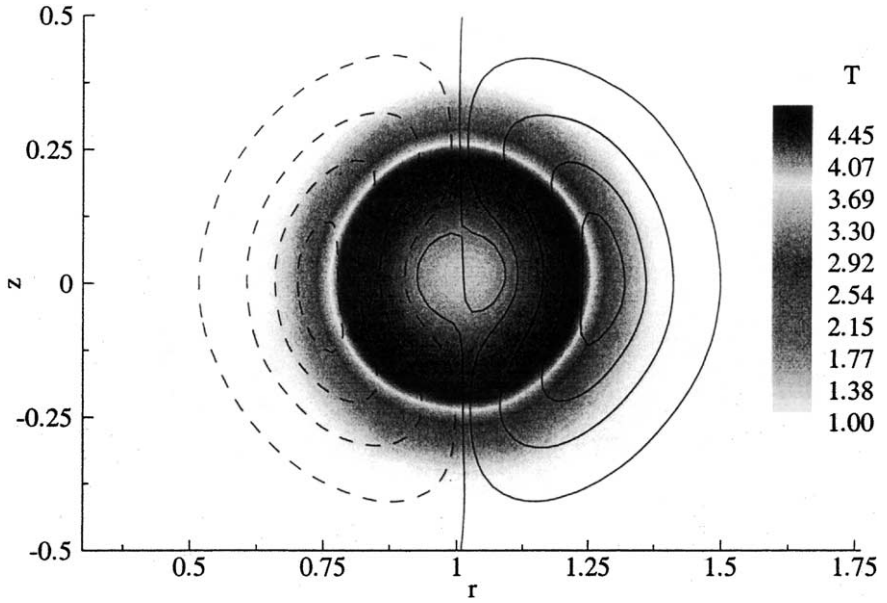

Fig. 15. Vorticity contours, shown in continuous line for positive values and broken lines for negative values, and temperature contours, shown in gray scale, at time 0.005, for the reacting ring problem. Absolute values for the vorticity are 0, 0.1, 0.05, 1, and 1.4.

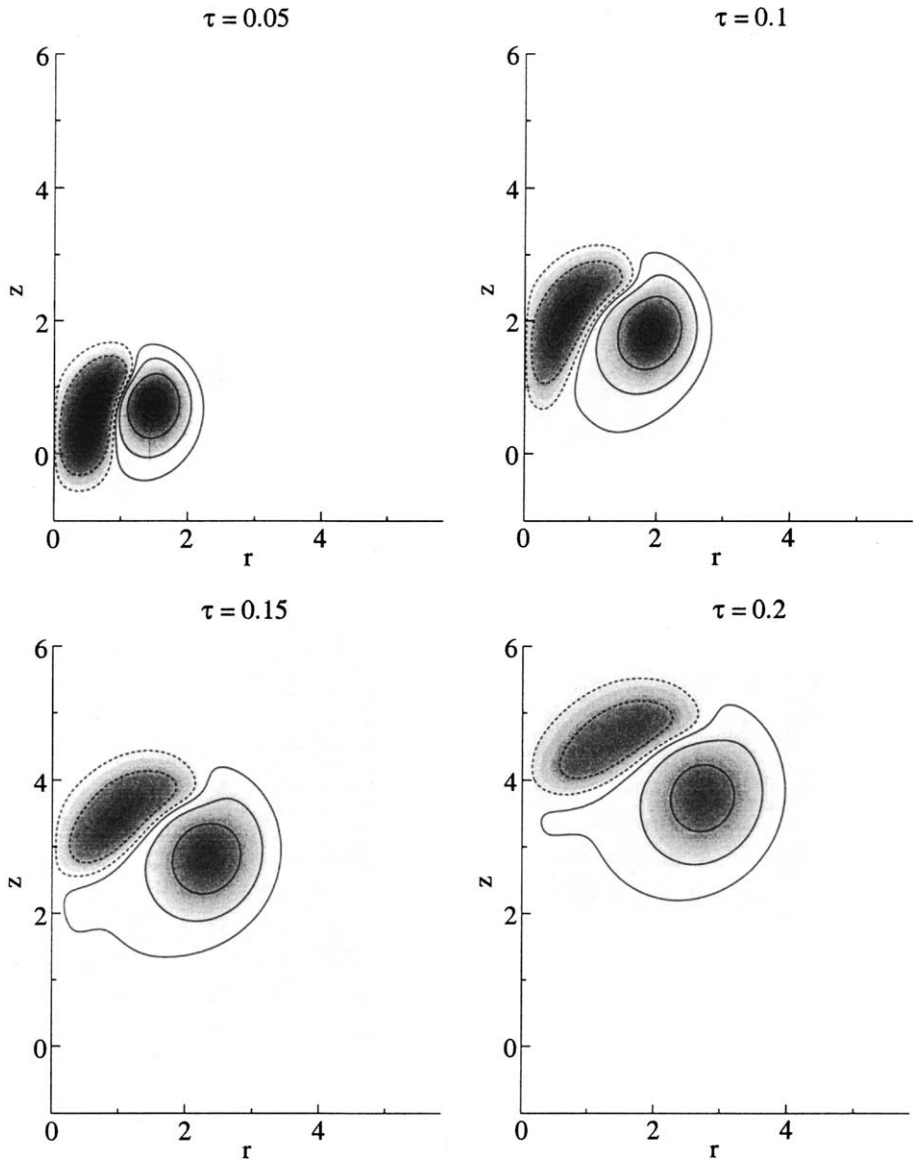

Fig. 16. Long time vorticity contours for the reacting ring problem, solid lines identify positive vorticity at values of 0.1, 0.5, 1.5, and 3. Broken lines correspond to negative vorticity of −0.1, −0.5, −1.5, and −2.5. Gray scale is used to distinguish between the contours.

symmetric distribution of the vorticity within the reacting core persists until decay across the centerline suppresses some of the negative circulation. This can be seen clearly in Fig. 17 where both the integrated negative, positive and total circulation are plotted vs. time. The positive and negative values grow at the same rate, keeping the total at almost zero until that time when the negative vorticity starts to decay due to diffusion across the centerline. The time of the onset of asymmetry could be predicted using the following argument. Since most vorticity is generated where the highest density gradient exists, which arises at the outer edges of the reacting ring whose initial radius is almost 0.5, and since the diffusion distance scales

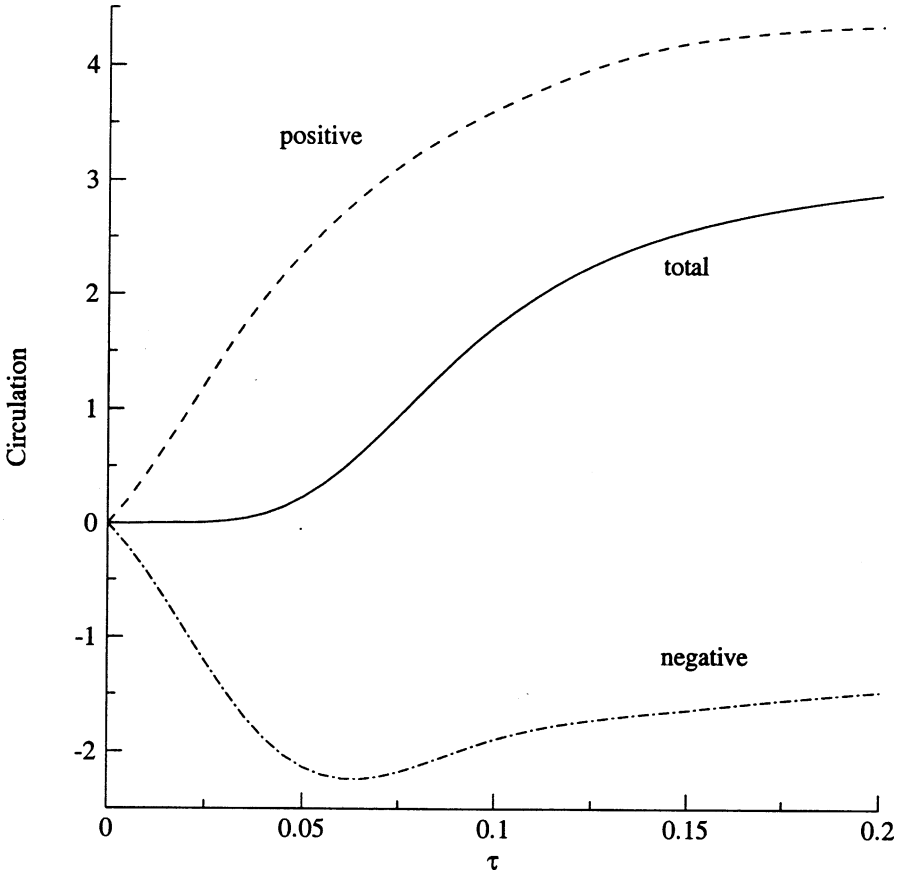

Fig. 17. The total circulation, and its negative and positive parts, for the case shown in Fig. 16.

with time as: $d \approx \sqrt{4\tau}$, it takes $\tau \approx 0.05$ for the vorticity to reach the axis of symmetry, in agreement with the simulation results. It is interesting that the rate of negative vorticity generation reaches zero around the same time, and starts to become positive again as the overall structure rotates such that less across-the-centerline-diffusion is observed. The rate of generation of net vorticity continues as long as some fuel remains in the reacting ring.

Temperature contours and a gray scale representation of the same variable are shown in Fig. 18. Even at the early stages, $\tau \approx 0.05$, the temperature distribution does not exhibit symmetry with respect to the ring center because of the asymmetric boundary conditions at the domain centerline, as argued before. The figure also shows the distortion experienced by the rising fuel/products ring as more fuel is burned, reflecting the impact of the vorticity asymmetry. It depicts how heat release induced volumetric expansion enlarges the area occupied by high temperature fluid beyond the initial extent of the fuel core, while the overall structure spins due to the dominance of the positive vorticity. Interestingly, the spinning tends to symmetrize the structure towards the latter stages, as seen at $\tau = 0.2$. It is also noticed that the high temperature contours migrate from the outer edges of the fuel ring towards the center as fuel is consumed, followed by diffusion.

The dependence of the solution on the numerical parameters, and, in particular, the time step, is demonstrated in Figs. 19 and 20, where the vorticity contours and the errors in vorticity and conserved

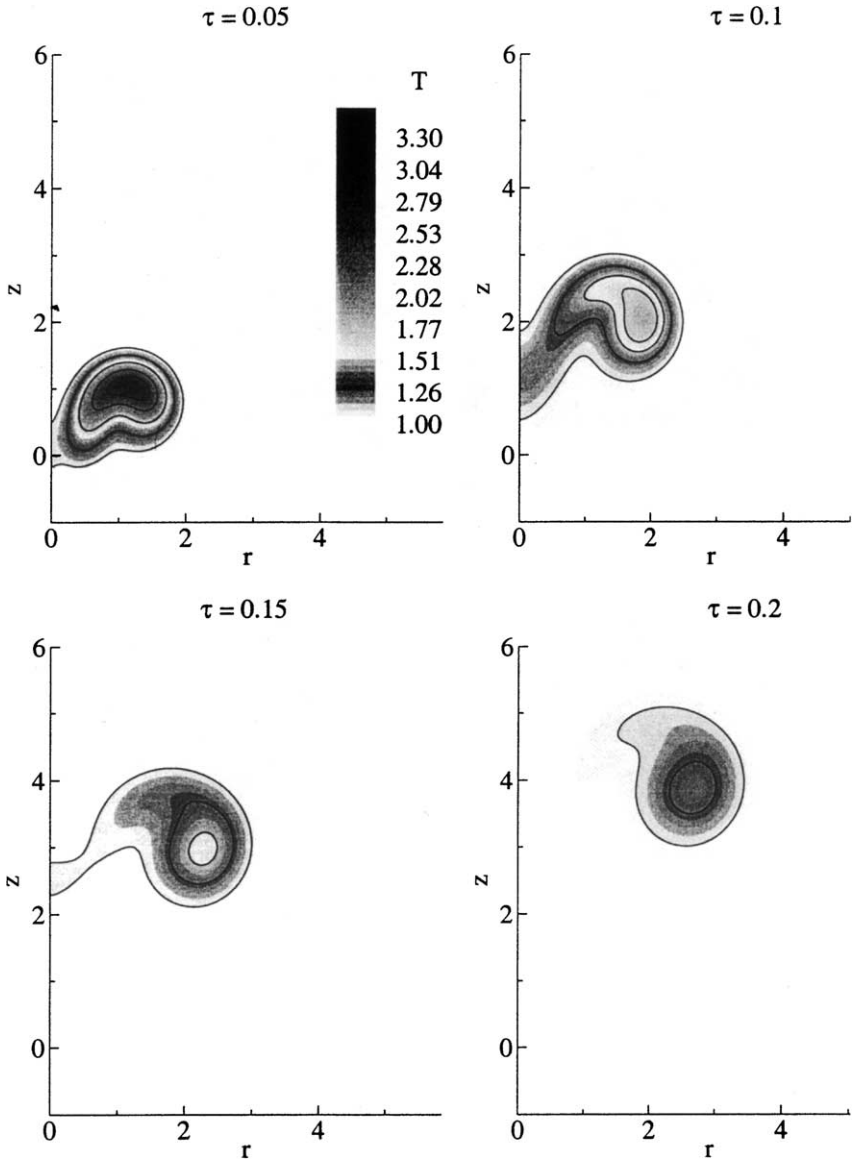

Fig. 18. The temperature contours for the case shown in Fig. 16, at the same times, the gray scale is used to define the absolute value of the temperature using a fixed scale.

scalar are shown, respectively. The former shows that the contours converge towards those obtained at the smallest time step as the time step is reduced, with the last simulations using the smallest time steps yielding almost the same contours. The L2 errors in the vorticity and scalar are computed using the solution at the smallest time step as the benchmark solution, i.e. the error is evaluated as the difference between the solution at an arbitrary time step and that obtained at the smallest time step, shows a dependence of $O(\overline{\Delta\tau}^{1.5})$. The super linear dependence on the time step is somewhat surprising, however, it is consistent with the results obtained before in the solution of the convection–diffusion problem.

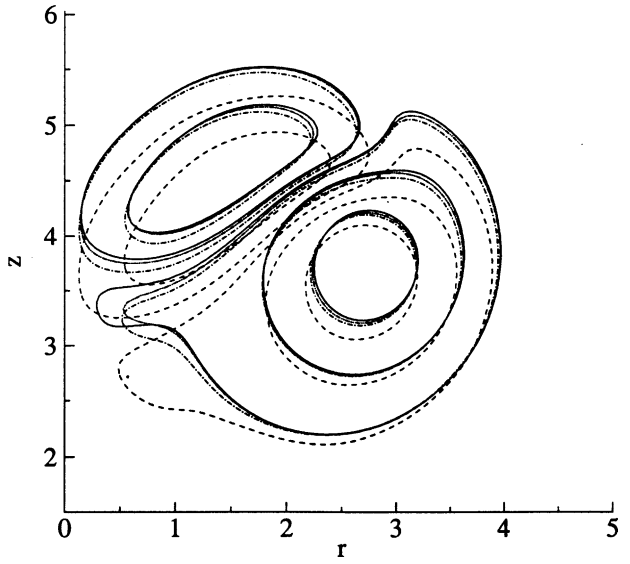

Fig. 19. Vorticity contours evaluated at the same final time, using different time steps, the vorticity values correspond to −2.5, −1.5, −0.5, −0.1, 0.1, 0.5, 1.5, and 3. The solid lines correspond to time step of 0.0005, dash–dot–dot lines to 0.001, dash-dot lines to 0.002, dashed line to 0.005.

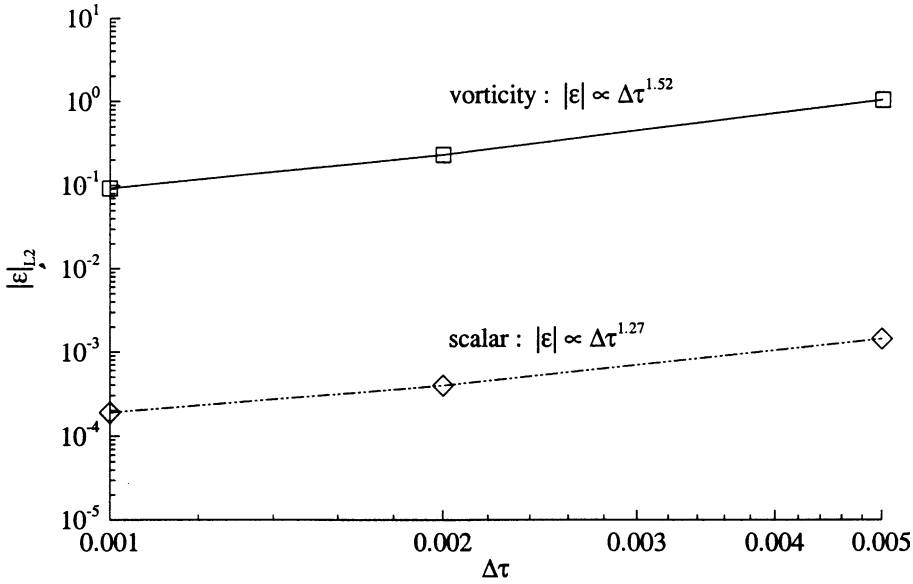

Fig. 20. The L2 errors in vorticity and scalar concentration as functions of the time step for the reacting ring problem.

5. Conclusions

The extension of the vortex methods to simulate reacting flow is not new, it has been attempted before using approximations in either the physical models, the numerical implementation or both. The work

presented here is taking these extensions a step further; by implementing an accurate solution of the diffusion equation, for both vorticity and conserved scalars, a compatible particle-based simulation of the scalar transport equations, and by maintaining the coupling with the compressible flow continuity equation. The latter imposes an extra velocity field due to the density variation following the chemical reaction. The density is computed form knowledge of the chemical species and temperature via the equation of state, with the former evaluated from the integration of the transport equations. The source terms are integrated at the locations of the vortex/scalar elements, and the strength of these elements is updated accordingly. The different terms in the transport equations are treated using operator splitting, and a predictor-corrector scheme is applied to integrate the source terms. Numerical results are used to study the convergence of the algorithms for a reacting compressible axisymmetric problem, following studies of the incompressible diffusion and convection–diffusion problems. For all cases attempted, careful refinement of the numerical parameters reduced the errors and led to convergent results.

For the diffusion problem we confirm a second-order convergence for the redistribution method in which an asymmetric core function is used, even when the formulation is limited to a first-order discretization, assuming nonuniform distribution of the computational elements. The improvement in the order seems to have been achieved because of the careful choice of the locations of the new elements, which guarantees almost uniform distribution around the diffusing element. Second-order convergence is established for both the distance between the elements and the core radius. The convection–diffusion scheme shows good accuracy, with second-order convergence as well in both spatial resolution and core size. Results support the significance of core overlap, $\delta/h > 1$, and are in agreement with the often-sited expression: $\delta^n + (h/\delta)^l \delta^2$, showing and optimal value of $1.5 < \delta/h < 2$. In the combustion application, a predictor corrector scheme is used to integrate the convection–generation part of the equations, and results exhibit super linear convergence.

Extension of this work is proceeding on different fronts, including the implementation of a redistribution method for variable diffusivity, the essence of which is the work of Shankar [18], the implementation of a fast solver and the solution of the finite rate kinetics problem.

Acknowledgements

This work was supported by the US Department of Energy, basic Energy Sciences, MICS, under contract DE-F602-98ER355. I.L. acknowledges the help and encouragement of Dr. S. Shankar.

References

[1] G.H. Cottet, P. Koumosetsakos, Vortex Methods: Theory and Practice, Cambridge University Press, New York, 2000.
[2] A. Krishnan, A.F. Ghoniem, Simulation of the rollup and mixing in Rayleigh Taylor flow using the vortex/transport element method, J. Comput. Phys. 99 (1992) 1–27.
[3] M. Soteriou, A.F. Ghoniem, Effect of free stream density ratio on free and forced spatially developing mixing layers, Phys. Fluids 7 (1995) 2036–2051.
[4] J. Ray, H.M. Najm, R.B. Milne, K.D. Devine, S. Kempka, Triple flame structure and dynamics aat the stabilization point of an unsteady lifted jet diffusion flame, Proc. Combust. Inst. 28 (2000) 219–226.
[5] A. Leonard, Computing three-dimensional incompressible flows with vortex elements, Annu. Rev. Fluid Mech. 17 (1985) 523.
[6] L. Cartolezzi, A.R. Karakozian, On the formation of the counter rotating vortex pair in transverse jets, J. Fluid Mech. 446 (2001) 347–373.
[7] J.C. Saghbini, A.F. Ghoniem, Simulation of the dynamics and mixing in swirling flow, In: 35th Aerospace Sciences Meeting, Reno, NV, January 1997, AIAA-97-0507.
[8] A.J. Chorin, Hairpin removal in vortex interactions, J. Comput. Phys. 91 (1990) 1–21.
[9] G.A. Sod, Automotive engine modeling with a hybrid random choice method, I and II, SAE Papers 790242 and 8000288, Detroit, MI, 1979.

[10] L.T. Martins, A.F. Ghoniem, Simulation of the nonreacting flow in a bluff-body burner; effect of the velocity ratio, J. Fluid Eng. 115 (1993) 474.
[11] E. Rivoalen, S. Huberson, Numerical simulation of axisymmetric viscous flows by means of a particle method, J. Comput. Phys. 152 (1998) 1–31.
[12] L. van Dommelon, A vortex redistribution technique, FMRL Report TR-3, Department of Mechanical Engineering, Florida State University, 1989.
[13] S. Shankar, L. van Dommelon, A new diffusion procedure for vortex methods, J. Comput. Phys. 127 (1996) 88–109.
[14] F.A. Williams, Combustion Theory, Addison-Wesley, New York, 1985.
[15] A. Majda, J. Sethian, The derivation and numerical solution of the equations for zero Mach number combustion, Combust. Sci. Technol. 42 (1985) 185–205.
[16] M. Soteriou, A.F. Ghoniem, Numerical simulation of exothermic, spatially developing shear flow, In: Proc. of the 2nd Int. Workshop on Vortex Flows and Related Numerical Methods, Montreal, Canada, August 1995, vol. 1, ENAIM, Proc., 1996, pp. 213–223. Available from <http://www.emath.fr/Maths/Proc/Vol.1/soteriou.htm>.
[17] J.T. Beale, A. Majda, Higher order accurate vortex methods with explicit velocity kernels, J. Comput. Phys. 58 (1985) 188–208.
[18] S. Shankar, Grid-Free Redistribution Methods for Axisymmetric Diffusion RGDL Report, Massachusetts Institute of Technology, Cambridge, MA, 1999.
[19] M. Nitsche, R. Krasny, A numerical study of vortex ring for motion at the edge of a circular tube, J. Fluid Mech. 276 (1994) 139–161.
[20] J.S. Marshall, J.R. Grant, A Lagrangian vorticity collocation method for viscous axisymmetric flows with and without swirl, J. Comput. Phys. 138 (1997) 302–330.
[21] A.F. Ghoniem, G. Hiedarinejad, A. Krishnan, Numerical simulation of a thermally stratified shear layer using the vortex element method, J. Comput. Phys. 79 (1988) 135–166.
[22] S. Shankar, A.F. Ghoniem, A redistribution method for axisymmetric diffusion, In: A. Giovannini, G.H. Cottet, Y. Gagnon, A.G. Ghoniem, E. Meiburg (Eds.), Vortex Flows and Related Numerical Methods III, Proceedings of the 3rd Int. Workshop, Toulouse, France, August 24–27, 1998, ESIAM, Proceedings, pp. 387–396. Available from <http://www.emath.fr/Maths/Proc/Vol.7/abs/shankar.html>.
[23] I. Lakkis, Numerical simulation of radiating fire plumes, Ph.D. Thesis, Massachusetts Institute of Technology, 2000.
[24] P.A. Reviant, Particle numerical models in fluid dynamics, In: K.W. Morton, M.J. Baines, Numerical Methods for Fluid Dynamics, Oxford, 1986, pp. 231–254.
[25] L.F. Rossi, Resurrecting core spreading vortex methods: A new scheme that is both deterministic and convergent, SIAM J. Sci. Comput. 17 (1996) 370–397.
[26] P. Degond, S. Mas-Galic, The weighted particle method for convection–diffusion equations, Part 1: the case of an isotropic viscosity, Math. Comput. 53 (1989) 485–507.
[27] J.P. Choquin, S. Huberson, Particle simulation of viscous flow, Comput. Fluids 17 (1989) 397–410.
[28] Y. Ogami, T. Akamatsu, Viscous flow simulation using the discrete vortex model – the diffusion velocity method, Comput. Fluids 19 (1991) 441–443.
[29] A. Gharakhani, A higher order vorticity redistribution method for 3D diffusion in free space, Sandia Report, SAND2000-2505.
[30] J.S. Marchall, J.R. Grant, Penetration of a blade into a vortex core: vorticity response and the unsteady blade forces, J. Fluid Mech. 103 (1996) 83–109.